

Numerical modelling of High-Speed Nailing process to join dissimilar materials: metal sheet formulation to simulate nail insertion stage

Fabien Goldspiegel, Katia Mocellin, Michel Philippe

▶ **To cite this version:**

Fabien Goldspiegel, Katia Mocellin, Michel Philippe. Numerical modelling of High-Speed Nailing process to join dissimilar materials: metal sheet formulation to simulate nail insertion stage. Journal of Materials Processing Technology, 2018. hal-01971423

HAL Id: hal-01971423

https://minesparis-psl.hal.science/hal-01971423

Submitted on 21 Oct 2021

HAL is a multi-disciplinary open access archive for the deposit and dissemination of scientific research documents, whether they are published or not. The documents may come from teaching and research institutions in France or abroad, or from public or private research centers.

L'archive ouverte pluridisciplinaire **HAL**, est destinée au dépôt et à la diffusion de documents scientifiques de niveau recherche, publiés ou non, émanant des établissements d'enseignement et de recherche français ou étrangers, des laboratoires publics ou privés.



Distributed under a Creative Commons Attribution - NonCommercial 4.0 International License

Version of Record: https://www.sciencedirect.com/science/article/pii/S0924013618304643
Manuscript_e7c085999136d5599c9c7e9657c11aee

Numerical modelling of High-Speed Nailing process to join dissimilar materials: metal sheet formulation to simulate nail insertion stage

Fabien Goldspiegel[1,2], Katia Mocellin[1], Philippe Michel[2]

[1] MINES ParisTech, PSL Research University, CEMEF, CNRS UMR 7635, CS 10207 rue Claude Daunesse, 06904 Sophia Antipolis Cedex, France
[2] Technocentre RENAULT, 1 avenue du Golf, 78288 Guyancourt Cedex, France

[a)] Corresponding author: fabien.goldspiegel@mines-paristech.fr
[b)] katia.mocellin@mines-paristech.fr
[c)] philippe.p.michel@renault.com

Abstract

Lightweigthing structures using mixed material components have become one of the main target of automotive industry future. In most cases, introduction of dissimilar materials leads to joining issues. Either materials can not be welded, due to thermal incompatibilities, neither joined by traditionnal plastic deformation-based processes (clinching, riveting,…) due to extended mechanical properties. New generations of Advanced High Strength Steels (AHSS) as well as boron steel have brought these joining processes to its limits. In this context, High-Speed Nailing is a very promising technology since a dynamic punch – working velocities up to 37 m/s - enables a wide range of materials to be joined - inclunding AHSS - in a short cycle time (10 ms) and is adapted to high production rate. However car manufacturers remain sceptical since joining mechanisms are not clearly understood and joint strength can not be predicted yet by engineering simulations. These considerations have driven the present work which proposes an insight into one of the main current issue of high-speed joining modelling: requirements on the material constitutive and damage laws to model fastener insertion stage. A step-by-step model construction methodology has been chosen here and applied to mixed materials configurations of dual-phase steel (1.5 mm-thick) and cast aluminium (2.5 mm-thick) joined in the two following superpositions: cast aluminium/steel and steel/cast aluminium. Strain and strain-rate dependant constitutive laws are calibrated on the basis of quasi-static and dynamic tests until strain rates up to 6000 s^{-1}. Two coupled-damage approaches are calibrated on both materials and applied to nailing simulations. Results are twofold: (1) whatever is the damage formulation, sheet reaction forces and fracture modes are well predicted by joining simulations; (2) upper and lower sheets fracture locations exhibit a distinct loading path, close to bi-axial state on the plane-stress locus for lower-sheet and mixed shear-tension state, out of the plane stress locus, for the upper sheet. Beyond the differences between damage formulations, simulations have established that critical damage parameter at fracture D_c has a major influence on nail insertion predictiliby, driving material ductility, therefore kinetic energy tranformed into plastic work.

1. Introduction
2. Material models
3. Material testings
4. Experimental nailings
5. Numerical simulations
6. Conclusions

Keywords

High-Speed joining, High strain-rate, Ductile damage, Numerical simulation, Material modelling

© 2018 published by Elsevier. This manuscript is made available under the CC BY NC user license
https://creativecommons.org/licenses/by-nc/4.0/

Main Text.

1. Introduction

Context

Environmental policies as well as growing stresses on fuel supply tend to be significant parameters in the design of future mechanical structures. Aerospace, railway, automotive industries have to evolve according to these new constraints without loss in the product quality. Hence, the automotive industry is challenged to find technological solutions to reduce global vehicle CO_2 emission per km. Restrictions are slightly different from one country to another, but it has became a worldwide concern which implies drastic changes in the manufacturing process. Among the solutions which have been explored by car manufacturers to reduce carbon dioxide emissions, the most relevant one consists in a multi-materials structure using lightweight materials. On one hand, materials with lower density would be promoted, such as alumimiun alloys, magnesium alloys, composites, for vehicle components which do not require high mechanical strengths. On the other hand, Advanced High Strength Steels (AHSS) would be added to stiffen parts subjected to very high stresses, and balance global loss of rigidity due to local changes from steel to softer materials. Use of metals with very high mechanical properties, such as AHSS, enables thinner parts than usual, which consequently induces once again mass savings.

Joining dissimilar materials

Materials with different chemical compositions and extended mechanical properties usually require joining solutions aside from joining processes. Meschut et al. (2014) showed that spot-welding incompatibility might appear between structural parts made of different materials. As consequences, the joining processes based on plastic deformation are investigated to fulfill both industrial requirements – limited preparation of the joining area, reliability, high industrial pace - and technical requirements – flexibility of the process parameters, wide range of join-able material configurations, high joint strengths. Among these processes, clinching, riveting and self-pierce riveting (SPR) have been used for long time in the industry for sheet metal applications on aluminium alloys and low strength steels but Mori et al. (2013) highlighted that it reached a limit with very high strength steels and low ductility materials. Thus, it has become a first order issue to adapt processes for materials with advanced properties. Optimizations were conducted on several parameters affecting join-ability, such as works of Abe et al. (2012) in which die shape is optimized to control plastic flow and delay crack occurrence, the works of Huang and Yanagimoto (2015) which propose thermally-assisted joining process to increase metal formability and the works of Meschut et al. (2014) which suggest to boost rivet material property to enable boron steel join-ability. In addition to these investigated parameters, Jäckel et al. (2014) revealed that an increasing tool velocity would improve blind rivet join-ability in a 22MnB5/6016 aluminium material superposition and get a cleaner sheet-rivet fracture interface.

From these considerations, several industrially-based research programs have tried to develop innovative joining solutions for automotive car bodies using material sensitivities to temperature and velocity to extend the range of process join-ability. Martinsen et al. (2015) and Groche et al. (2014) have proposed overviews of the most popular processes used to join dissimilar materials: Friction Stir Blind Riveting (FSBR), Self-Piercing Punch Riveting (SPPR), Flow-Drilling Screw (FDS)... As stated by Chastel and Passemard (2014),some of these technologies have become really attractive for industrial applications since neither pre-hole nor additional support are required but only one side access for the setting tool.

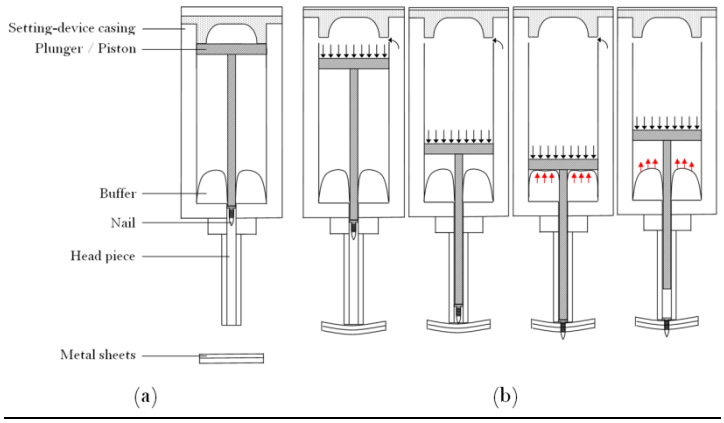


Figure 1: (a) Main components of the nail-setting device
(b) Joining process divided in 5 main steps: 1) Piston initial position; 2) Piston acceleration; 3) Nail/Sheet contact; 4) Damping; 5) Piston oscillations (Goldspiegel et al., 2017)

High-speed nailing process

The process under investigation in the present paper is one these promising technologies used for multi-materials applications to join highly dissimilar materials. It is called High-Speed Nailing (HSN) and works at relatively high tool velocity (17 to 37 m/s) to extend the materials perforation-ability and therefore the range of materials join-ability. It consists in a pneumatic-driven piston used to punch a nail into several material layers. The founding principles of nailing as an industrial joining process have been established in the works of Draht (2006) in which both nailing device technology and nailed-joint properties have been investigated. Hußmann (2008) refined nailed-joint industrial applicability with mechanical tests on mono and multi-points samples taking into account different sheet materials stiffness, inter-sheets glue, corrosion and also experiments on fatigue bench. The investigations regarding nailed-joint validity have been continued in the works of Flüggen and Hahn (2010) through applications on aluminium profiles and composites. Results from local bending measurements in the nail surrounding area, joint strengths and also failure modes are discussed.

As the joining technology has become more understandable by researchers and engineers, it has been adapted to industrial applications with high production rates. Consequently the nailing device has been set on a robot, as it can be seen in Figure 1 (a), and the joining cycle is controlled by a sequence of five main steps, presented in Figure 1 (b), described as follows: when air flows into the main chamber, the piston is accelerated downwards until velocities up to 37 m/s to provide enough impact kinetic energy for joining. A buffer is located at the bottom of the chamber to stop piston when kinetic energy is in excess. As a nail is placed at the piston tip, it follows piston motion. When piston approaches bottom chamber limit, the maximum velocity is reached and nail starts to contact the upper-sheet. As it progresses into the sheets, both piston and nail velocity decrease. Piston kinetic energy is mainly transformed into plastic work until piston contacts the buffer. It damps piston motion until springback effect propels piston upwards. After several oscillations the piston goes back to initial position to be ready for the next joining cycle.

Numerical simulation of the fastener insertion stage

Due to continuous interest for light-weighting solutions in the industry, engineers in charge of joining applications keep claiming for a quick and reliable tool to facilitate the decision-making process. Numerical simulations of joining processes have proven that sheet materials reaction to the fastener insertion as well as in-service joint strength can be accurately predicted if appropriate material constitutive and damage laws are used. Porcaro et al. (2006) and Carandente et al. (2016) have simulated the insertion of a self-piercing rivet into a double aluminium-layers configuration with good agreement on the force-displacement tool history. In both configurations the upper-sheet failure was modelled through a geometrical-based criterion which triggers mesh

separation when a given distortion value is reached. Authors like Cacko (2008) , Bouchard et al. (2008) and Fayolle (2009) have preferred to use a physical-based Lemaitre formulation to model the upper sheet fracture by rivet tip descent. It was shown that accounting for damage did not affect the insertion stage but it significantly improved the joint strength prediction. Zhao et al. (2014) have followed similar trend than previous authors with a coupled-damage Rousselier formulation to predict the failure behavior of a clinched joint. However most authors have chosen to model sheets damage under uncoupled formulation with only a fracture criterion. Lee et al. (2014) used a Cockroft and Latham (CL) criterion to investigate DP780 neck fracture in hole-clinching process simulations, Mucha (2014) also used a CL criterion on steel/aluminium superposition joined with a SPR-solid rivet whereas Lambiase and Di Ilio (2016) used a Rice and Tracey criterion to predict the onset of crack and propagation into clinched-joints made of aluminium plates.

For most traditional joining process simulations, the main concern is to properly model metal flow inside the dies without considerations on damage. In these cases an uncoupled fracture criterion was sufficient to account for crack occurrence. But in the new generation of joining processes, such as High-Speed Nailing, Spin-Blind Riveting or even Flow-Drilling Screw, every materials layers have to be perforated before being joined. Then sheets failure modelling becomes mandatory to get realistic sheets reaction as well as final interface geometry and therefore it has to be assessed by an appropriate damage evolution law. Wiethop (2010) discussed the importance of the fracture criterion in punch riveting simulations using Simufact software. Results obtained with a geometrical-based criterion have shown good agreement on cross-section comparisons of ductile joined materials. But used on high-strength steels, this criterion was considered inappropriate to simulate the sheets failure pattern. A first attempt to use physical-based fracture criterion can be found in the works of Kaboli et al. (2015) in which a Johnson-Cook criterion is used to simulate the penetration stage of a spin-blind riveting process on a magnesium alloy/composite superposition. Recently Goldspiegel et al. (2017) and also Folgar Ribadas et al. (2017) presented advanced numerical simulations of High-Speed Nailing process using Johnson-Cook criterion. All these works have mentioned similar issues regarding fracture modelling in the fastener penetration stage: in addition to unrealistic sheets fracture mode obtained by simulations, an important volume loss is noticed by use of either an excessive elements deletion or an inappropriate damage law.

From these considerations, the present work target is twofold: (1) to propose a step-by-step material characterization methodology for sheets perforation-based joining processes; (2) to model High-speed nailing of mixed aluminium-steel configurations and give an insight into the mechanical phenomena which occur during the nail insertion stage. Hence dissimilar materials have been selected to be as close as possible to multi-material structure applications and tested in the two following upper-sheet/lower-sheet configurations: cast aluminium (2.5 mm)/dual-phase steel (1.5 mm) and dual-phase steel (1.5 mm)/cast aluminium (2.5 mm). In the first part, material constitutive and damage formulations are proposed to account for both nail and sheets mechanical behavior during penetration and perforation steps of the joining process. Then mechanical tests are conducted on these materials for model calibration. The second part presents experimental nailing tests on instrumented frame to provide valuable references for further comparison with simulations. The third part introduces inputs of the joining simulation and finally, results are discussed in terms of piston kinematics, fracture modes and geometrical discrepancies.

2. Material models

Two sheet materials and only one nail material are considered in this article. Chemical composition of these materials are presented in Table 1 whereas Table 2 gives their main mechanical features. Steel is provided by Arcelor Mittal, under the commercial name DP780 in 1,5 mm-thick sheet without any coat. Due to the forming process, rolling may have generated microstructural anisotropy and will be check in further section 3.1.1. Cast aluminium were produced in a 90 mm x 190 mm rectangular ingot before T6-heat treatment had been processed. No investigation regarding cast aluminium anisotropy was possible because of incompatibility between ingots sizes and specimen – specimen length is 120 mm whereas lingot width is 90 mm . However, authors have found no reason which could legitimate any anisotropy in the molted material since (1) no particular direction is promoted during the forming step and (2) no significant irregularity in the microstructure would withstand the final heat treatment. Consequently, isotropy will be considered for cast aluminium in the rest of this article. The

last material of interest is the nail one. It is made from C60 steel and forged through several steps until final nail shape could be obtained. At the end, a Zn-Ni based coating is performed on the nail surface to prevent from in-service corrosion.

Table 1

Table 2

In the following are examined constitutive models applied to both nail and sheet materials whereas damage formulations will only be considered for sheets. Before going through these models, few notions which going to appear all along this article have to be presented at first.

2.1 Stress-state parameters

To account for metal plasticity and damage models three invariants (Eq. (1), Eq. (2) and Eq. (3)) of the stress tensor σ need to be introduced:

	$p = -\sigma_h = -\frac{1}{3}(\sigma_I + \sigma_{II} + \sigma_{III}) = -\frac{I_1}{3}$	(1)
	$q = \bar{\sigma} = \sqrt{\frac{1}{2}[(\sigma_I - \sigma_{II})^2 + (\sigma_{II} - \sigma_{III})^2 + (\sigma_{III} - \sigma_I)^2]} = \sqrt{3J_2}$	(2)
	$r = \left[\frac{27}{2}(\sigma_I - \sigma_h)(\sigma_{II} - \sigma_h)(\sigma_{III} - \sigma_h)\right]^{\frac{1}{3}} = \left(\frac{27}{2}J_3\right)^{\frac{1}{3}}$	(3)

where $\sigma_I \geq \sigma_{II} \geq \sigma_{III}$ are the ordered principal stresses. The stress-state can be uniquely described by the three invariants p, q, r – also expressed I_1, J_2, J_3 - or by two dimensionless parameters, the stress triaxiliality σ^* in Eq. (4) and the Lode parameter μ_σ in Eq. (5) defined as :

	$\sigma^* = \frac{\sigma_h}{\bar{\sigma}}$	(4)
	$\mu_\sigma = \frac{2\sigma_{II} - \sigma_I - \sigma_{III}}{\sigma_I - \sigma_{III}}$	(5)

where $\bar{\sigma}$ is the equivalent stress and σ_h the hydrostatic stress. The Lode parameter is also used under the form of the Lode angle θ_L or the Lode angle parameter $\bar{\theta}(-1 \leq \bar{\theta} \leq 1)$ respectively written $\theta_L = \tan^{-1}\left(\frac{1}{\sqrt{3}}\mu_\sigma\right)$ and $\bar{\theta} = -\frac{6}{\pi}\theta_L$.

2.2 Yield function

Since the main feature of the High-Speed Nailing process is dynamics and investigated materials are metals, it has been stated that both nail and sheets will be modelled with an elastic-visco-plastic behavior. Every elastic parameters are presented in Table 2. However it is usually accepted that elasticity has a limited influence on the response of a material which undergoes dynamic loading - i.e. high strain-rate – and large strains. The elastic work becomes negligible regarding plastic work and almost the entire material response is driven by yield stress. Johnson and Cook (1983) performed taylor impact tests on three different metals and stated that under high strain rates, material may experience significant variations in yield stress. All exhibits a strain-rate hardening and a thermal softening when loading velocity and temperature were increased. These authors found that changes in material yield stress can be reasonnably predicted with a linear dependence on temperature and a natural

logarithm dependence on the strain-rate. This formulation has been widely used afterwards, in industrial or research-based programs, to treat material response subjected to dynamic loadings. However, the Johnson-Cook formulation (Eq. (10)) - called JC model - has been highly contested due to its phenomenological origin. Used for impact applications, Børvik et al. (2003) considered this formulation particularly unadapted to represent material response under high temperature, such as blue brittleness effect. To overcome such issues, Zerilli (2004) proposed a thermally-based model – called ZA model - to explain hardening as a mechanism of dislocation motions. Dey et al. (2007) conducted simulations of steel-plate perforation by ballistic projectile to compare JC and ZA constitutive models. It was concluded that, for impact velocities close to the ballistic limit, i.e. velocity threshold between non-penetration and full penetration of a plate with a given set of boundary conditions, JC relation predicts considerably better both ballistic limit velocity and crack fracture path than ZA. JC formulation with cumulative effect of strain, strain-rate and thermal sensitivities remains the most practical for parameters identification. This reason explains why this constitutive law has spread among engineers and why it will be used hereafter on the three selected materials.

Assuming materials isotropy, a thermo-dynamical Von Mises yield function (see Eq. (7)) was considered appropriate to account for the material sensitivities previously mentionned:

$$f = \bar{\sigma}(\sigma) - w(D).\sigma_Y(\bar{\varepsilon}_{pl}, \dot{\bar{\varepsilon}}_{pl} T) \quad (7)$$

where σ_Y is the yield stress and $w(D)$ is the weakening function in order to take into account damage softening when the isotropic damage scalar D is calculated as an internal variable $(0 \leq D \leq 1)$. A convenient interpretation of damage uses the ratio of damaged area S_D to the total surface S such as: $D = S_D/S$. The effective stress tensor $\tilde{\sigma}$ is used as the one which should be applied to an undamaged material, in order to get the same elastic strain tensor as the one obtained from the undamaged material under actual stress σ . It has been formulated in the works of Lemaitre and Chaboche (1994) and is called strain equivalence principle, as expressed in Eq. (8):

$$\tilde{\sigma}_{ij} = \frac{\sigma_{ij}}{1 - D} \quad (8)$$

where $\tilde{\sigma}_{ij}$ and σ_{ij} are respectively components of the effective stress tensor and of the actual stress tensor. The weakening function $w(D)$ - presented in Eq. (9) - is based on this principle and affects macro-mechanical behavior in a different way if material is rather in a dominant compression stress-state $(\sigma^* < 0)$ than in a tension stress-state $(\sigma^* \geq 0)$:

$$w(D) = \begin{cases} (1 - hD^{\beta}) & if \quad \sigma^* < 0 \\ (1 - D^{\beta}) & if \quad \sigma^* \geq 0 \end{cases} \quad (9)$$

where h is a material parameter $(0 < h < 1)$ which accounts for micro-crack closure effect. Lemaitre and Chaboche (1994) have found from tension and compression tests that parameter h equals to 0.2 is assumed valid for most materials. This parameter will be taken to 0.2 for both selected materials of this article. According to this weakening function, the effective stress tensor under compression is reformulated as : $\tilde{\sigma}_{ij} = \sigma_{ij}/(1 - hD)$. The weakening exponent β is a calibration parameter – in the original Lemaitre formulation $\beta = 1$ – which enables to extend damage effect on mechanical behavior under a more general formulation. The set of equations Eq. (7), Eq. (8), Eq. (9) composed the formulation which has been chosen in this article to cover two coupled damage approaches of interest: Lemaitre damage model (LEM) and phenomenologically-based damage model (PB). It means that both LEM and PB approaches will use the same coupling formulation – accounting for micro-crack closure effect and damage softening – but damage D will be calculated according to the inherent model formulation.

Following the Johnson and Cook (1983) formulation, constitutive law is written under a multiplicative form such as Eq (10):

$$\sigma_Y\left(\bar{\varepsilon}_{pl}, \dot{\bar{\varepsilon}}_{pl}, T\right) = k_1\left(\bar{\varepsilon}_{pl}\right) k_2\left(\dot{\bar{\varepsilon}}_{pl}\right) k_3(T) \quad (10)$$

with the strain hardening term k_1 (Eq(10.1)):

$$k_1\left(\bar{\varepsilon}_{pl}\right) = \Lambda\, k_S\left(\bar{\varepsilon}_{pl}\right) + (1-\Lambda)\, k_V\left(\bar{\varepsilon}_{pl}\right) \quad (10.1)$$

with k_S and k_V which are respectively the strain hardening Swift (Eq(10.11)) and Voce (Eq(10.12)) formulations and Λ the balance parameter.

$$\begin{cases} k_S\left(\bar{\varepsilon}_{pl}\right) = \lambda_1\left(\bar{\varepsilon}_{pl} + \bar{\varepsilon}_0\right)^{\lambda_2} & (10.11) \\ k_V\left(\bar{\varepsilon}_{pl}\right) = \lambda_3 + \lambda_4\left(1 - \exp\left(-\lambda_5\, \bar{\varepsilon}_{pl}\right)\right) & (10.12) \end{cases}$$

Strain-rate hardening is modelled through a Johnson-Cook based term k_2 (Eq(10.2)):

$$k_2\left(\dot{\bar{\varepsilon}}_{pl}\right) = 1 + \beta_{eq} \ln\left(\frac{\dot{\bar{\varepsilon}}_{pl}}{\dot{\bar{\varepsilon}}_0}\right) \quad (10.2)$$

with $\dot{\bar{\varepsilon}}_0$ the referent strain-rate established from quasistatic tensile test and the non-linear sensitivity to the strain-rate $\beta_{eq} = \beta_1\left(\dot{\bar{\varepsilon}}_{pl}/\dot{\bar{\varepsilon}}_0\right) + \beta_2$ such that if $\beta_1 = 0$, it reduced to the original Johson-Cook formulation. Finally the thermal softening effect is modelled through the term k_3 (Eq(10.3)) with parameters T_0 for reference temperature, T_m for melting temperature and the thermal sensitivity exponent θ_1:

$$k_3(T) = 1 - \left(\frac{T - T_0}{T_m - T_0}\right)^{\theta_1} \quad (10.3)$$

2.3 Damage formulation

In the present work we have considered that a coupled-damage approach would be really convenient to model ductile fracture in high-speed nailing applications. On one hand, it would avoid the important volume loss noticed with the use of uncoupled damage formulation in which element deletion is triggered when a critical value is reached. On the other hand, the use of a physical-based damage evolution law would promote realistic damage growth and strain localization inside the metal sheets. Consequently the kill-element procedure would be restricted to few elements located in the crack onset area where damage and element distorsion are maximum. It makes this innovative approach really interesting since it preserves the interface between nail and sheets from excessive element deletion and therefore it enables nailed-joint testing simulation from result of the joining stage.

The Lemaitre (LEM) and Phenologically-based (PB) formulations, chosen to model damage in the joining simulation, will be introduced in the following sections.

2.3.1 Lemaitre (LEM) damage approach

On the basis of continuum mechanics, Lemaitre and Chaboche (1994) proposed a theory in which damage growth is driven by the total elastic work w_{el} dissipated into the material (sum of distorsion energy and hydrostatic energy). A driving force Y is assumed – called Energy density release rate – and expressed as (see Eq. (11)):

$$Y = \frac{1}{2}\frac{dw_{el}}{dD}\bigg|_{\sigma,T} = \frac{h\bar{\sigma}^2}{2E(1-hD)^2}\cdot R_v \quad (11)$$

with a constant stress σ and temperature T, with E and ν which are respectively Young modulus and Poisson ratio and the function of stress-triaxiality $R_v = \frac{2}{3}(1+\nu) + 3(1-2\nu)\sigma^{*2}$. From the consideration of a damage dissipative potential, damage evolution rate is written in Eq. (12) as:

$$\dot{D} = \begin{cases} 0 & if \quad \bar{\varepsilon}_{pl} < \bar{\varepsilon}_D \; or \; \sigma^* < -\frac{1}{3} \\ \left(\frac{Y}{S}\right)^b \dot{\bar{\varepsilon}}_{pl} & if \quad \bar{\varepsilon}_{pl} \geq \bar{\varepsilon}_D \end{cases} \quad (12)$$

with S and b which are material parameters, the exponent b usually taken as $b = 1$ for alumimium alloys and $b = 2$ for steels as detailed in Lemaitre and Chaboche (1994). In addition to the works Bao and Wierzbicki (2005) - in which a cut-off value is assumed to avoid damage growth under dominant compression stress-state – an other condition, based on the minimum value of effective plastic strain before damage can occur, is introduced in Eq. (13). Under the formulation proposed in the works of Cao et al.(2014) and written in Eq. (13), the effective plastic strain threshold $\bar{\varepsilon}_D$ can variate with stress-triaxiality σ^*as:

$$\bar{\varepsilon}_D = \bar{\varepsilon}_{D0}\exp(-k.\sigma^*) \quad (13)$$

where $\bar{\varepsilon}_{D0}$ and k are material parameters. In the present work, an additional formulation of the equivalent strain threshold $\bar{\varepsilon}_D$ is used (Eq.(14)). This exponential form has been extended to four different threshold values $\bar{\varepsilon}_{D1}$, $\bar{\varepsilon}_{D2}$, $\bar{\varepsilon}_{D3}$, $\bar{\varepsilon}_{D4}$ which have to be calibrated from experiments and are assessed to the range of stress-triaxiality ${\sigma^*}_1$, ${\sigma^*}_2$, ${\sigma^*}_3$, ${\sigma^*}_4$. This is pictured as a locus in Figure 2. For conveniency, parameters are calculated as $k_{12} = -\ln(\bar{\varepsilon}_{D2}/\bar{\varepsilon}_{D1})/({\sigma^*}_2 - {\sigma^*}_1)$, $k_{23} = -\ln(\bar{\varepsilon}_{D3}/\bar{\varepsilon}_{D2})/({\sigma^*}_3 - {\sigma^*}_2)$ and $k_{34} = -\ln(\bar{\varepsilon}_{D4}/\bar{\varepsilon}_{D3})/({\sigma^*}_4 - {\sigma^*}_3)$.

$$\bar{\varepsilon}_D = \begin{cases} \bar{\varepsilon}_{D1} \quad if \quad \sigma^* < {\sigma^*}_1 \\ \bar{\varepsilon}_{D1}\exp(-k_{12}.\sigma^*) \quad if \quad {\sigma^*}_1 \leq \sigma^* < {\sigma^*}_2 \\ \bar{\varepsilon}_{D2}\exp(-k_{23}.\sigma^*) \quad if \quad {\sigma^*}_2 \leq \sigma^* < {\sigma^*}_3 \\ \bar{\varepsilon}_{D3}\exp(-k_{34}.\sigma^*) \quad if \quad {\sigma^*}_3 \leq \sigma^* < {\sigma^*}_4 \\ \bar{\varepsilon}_{D4} \quad if \quad \sigma^* < {\sigma^*}_4 \end{cases} \quad (14)$$

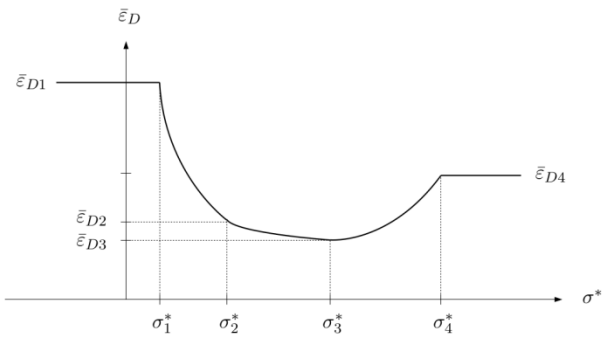


Figure 2: Modified effective strain threshold triggering damage accumulation presented as a locus

2.3.2 Phenomenologically-based (PB) damage approach

The phenomenologically-based damage model is based on considerations that damage scalar variable D $(0 \leq D \leq 1)$ (see Eq. (15)) can be simply expressed as:

$$D = \left(\frac{\bar{\varepsilon}_{pl}}{\bar{\varepsilon}_f}\right)^m \quad (15)$$

where $\bar{\varepsilon}_f$ is the effective plastic strain at fracture and m is a non-linear damage evolution exponent. For the same reasons than in Lemaitre formulation, damage growth is driven by a stress-state condition ($\sigma^* \geq -1/3$) and an effective plastic strain threshold ($\bar{\varepsilon}_{pl} \geq \bar{\varepsilon}_D$) as expressed in Eq. (16):

$$\dot{D} = \begin{cases} 0 & if \quad \bar{\varepsilon}_{pl} < \bar{\varepsilon}_D \; or \; \sigma^* < -\frac{1}{3} \\ m\left(\frac{1}{\bar{\varepsilon}_f}\right)\left(\frac{\bar{\varepsilon}_{pl}}{\bar{\varepsilon}_f}\right)^{m-1} \dot{\bar{\varepsilon}}_{pl} & if \quad \bar{\varepsilon}_{pl} \geq \bar{\varepsilon}_D \end{cases} \quad (16)$$

This formulation is really convenient since damage can be related to any desired physical dependancies and modelled throught the function – also called fracture locus - $\bar{\varepsilon}_f = f(\sigma^*, \mu_\sigma, \dot{\bar{\varepsilon}}_{pl}, T, \dots)$.

2.4 Fracture loci

In the present section, several phenomenologically-based criteria have been investigated to be used under the coupling formulation introduced in Eq. (16). Fracture loci are built from effective plastic strains at fracture obtained from mechanical tests conducted at different stress-states, i.e. for a given set of stress-state parameters $\{\mu_\sigma; \sigma^*\}$, and are formulated as follows:

- Cockroft-Latham (CL)

On the basis of the work of Cockroft and Latham (1968) in which a critical plastic work at fracture F_3 is assumed, this criterion has been extended with two additional parameters F_1 and F_2 to enable a better flexibility to the stress-state dependancy. Gruben et al. (2012) has used this extended form of the criterion on dual-phase steel and is presently expressed in Eq. (17), in the stress-state space, i.e $\bar{\varepsilon}_f = \{\sigma^*; \mu_\sigma\}$, such as:

$$\bar{\varepsilon}_f{}^{CL} = \frac{F_3 \, D_c}{\bar{\sigma}} \left\langle \frac{F_1\left(3\sigma^*\sqrt{3+{\mu_\sigma}^2} - 3 - \mu_\sigma\right) + 6}{3\sqrt{3+{\mu_\sigma}^2}} \right\rangle^{-F_2} \quad (17)$$

where $\langle \dots \rangle$ are the Macaulay brackets, $0 \leq F_1 \leq 1$, $F_2 \geq 0$ and $F_3 \geq 0$. This criterion reduces to the original Cockroft-Latham (CL) criterion - $F_3 = \int \langle \sigma_I \rangle \, d\bar{\varepsilon}_{pl}$ - when $\{F_1 = 1; \; F_2 = 1\}$.

- Bai-Wierzbicki (BW)

Bai and Wierzbicki (2008) proposed a fracture locus using three intermediate functions $\bar{\varepsilon}_f{}^{(+)}$, $\bar{\varepsilon}_f{}^{0}$ and $\bar{\varepsilon}_f{}^{(-)}$ – respectively for Generalized compression state $(\mu_\sigma = +1)$, Generalized shear state $(\mu_\sigma = 0)$ and Generalized tension state $(\mu_\sigma = -1)$ - to build a Lode-dependent function, such as expressed in Eq. (18):

$$\bar{\varepsilon}_f{}^{BW} = \left[\frac{1}{2}\left(\bar{\varepsilon}_f{}^{(+)} + \bar{\varepsilon}_f{}^{(-)}\right) - \bar{\varepsilon}_f{}^{0}\right]{\mu_\sigma}^2 + \frac{1}{2}\left(\bar{\varepsilon}_f{}^{(+)} - \bar{\varepsilon}_f{}^{(-)}\right)\mu_\sigma + \bar{\varepsilon}_f{}^{0} \quad (18)$$

where $\bar{\varepsilon}_f{}^{(+)} = F_1 \exp(-F_2.\sigma^*)$, $\bar{\varepsilon}_f{}^{0} = F_3 \exp(-F_4.\sigma^*)$ and $\bar{\varepsilon}_f{}^{(-)} = F_5 \exp(-F_6.\sigma^*)$. In the present work, two versions of this criterion are presented : one with symmetry between compression and tension stress-state $(F_5 = F_1; \; F_6 = F_2)$ – written as BW4P in the following – whereas the other one is asymmetrical, written BW6P.

3. Material testings

The calibration of yield stress and damage models, identified in section 2.2, 2.3 and 2.4, requires experimental data obtained from mechanical tests. They are conducted on sheets and nail for various specimen geometries, loading conditions and strain rates. These tests are detailed in the following sections.

3.1 Sheet materials characterization

3.1.1 Uniaxial tensile tests

Standards recommendations from the International Organization for Standardization (2009) have been respected to machine nine specimens from steel sheets for three different angles to the rolling direction. Three tests were performed at each angle 0°, 45° and 90° in quasi-static conditions at a velocity of 5 mm/min to get a mean strain-rate until necking of $\dot{\bar{\varepsilon}}_0 = 5.10^{-4} s^{-1}$. As shown in Figure 3, the force-displacement curves from 3 different angles give very similar results. It attests that rolling process has no significant effect on this material yield surface.

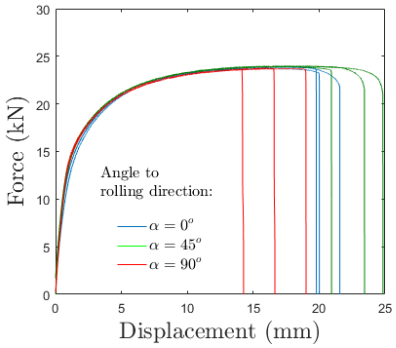


Figure 3: Uniaxial tensile tests performed on steel (DP780) at different angle to the rolling direction: 0°, 45° and 90°

To quantify this yield-stress anisotropy, a ratio r_α can be defined at each angle α to the rolling direction (see Eq. (19)) and for a given state of equivalent plastic strain $\bar{\varepsilon}_{pl}$. It is expressed as:

$$r_\alpha = \left.\frac{\sigma_Y^\alpha}{\sigma_Y^{0°}}\right|_{\bar{\varepsilon}_{pl}} \quad (19)$$

where $\sigma_Y^{0°}$ is the reference yield stress at $\alpha = 0°$ and σ_Y^α the yield stress at the angle α. These ratio have been evaluated for plastic strain from $\bar{\varepsilon}_{pl} = 0.02$ to $\bar{\varepsilon}_{pl} = 0.1$. Results are gathered in Table 3. Even if r_α-value slighly changes with the plastic strain, no significant difference can be noticed and it remains close to 1. Consequently we have considered that yield-stress anisotropy could be neglected in this study and that isotropic assumption is consistent for DP780 steel behavior.

Table 3

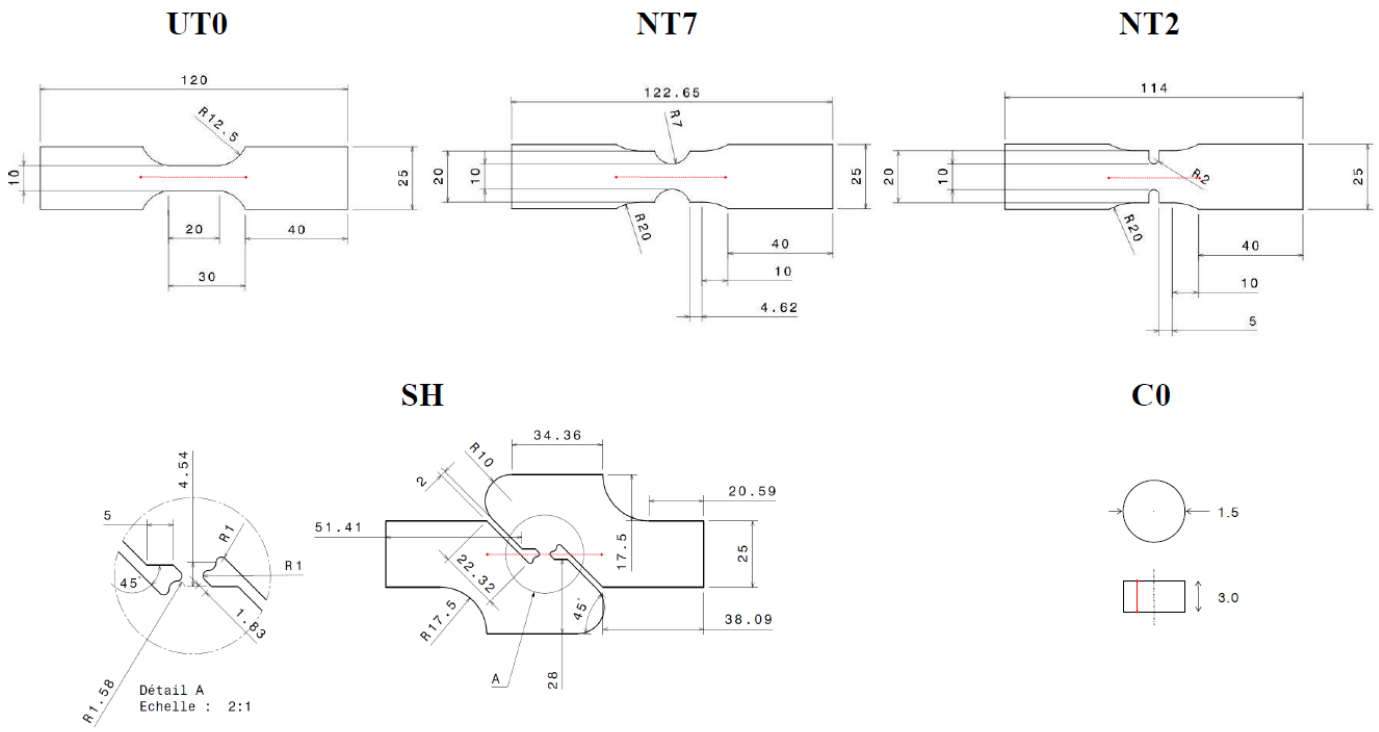


Figure 4: Specimens used for mechanical tests (tension for UT0, NT7, NT2, SH and compression for C0)

3.1.2 Notched tensile tests

Bridgman (1952) was the first to demonstrate, later verified in the works of Bao and Wierzbicki (2004) and a tremendous amount of authors, that notched specimens subjected to tension induce inside the material thickness a stress-triaxiality magnitude σ^* which can be related to the notched radius. However, as in the present case only sheet materials are concerned, possible stress-states are limited to configurations which satisfy plane stress condition, which means that evolution of Lode angle parameter $\bar{\theta}$ can not be considered apart from stress-triaxility σ^*, and is related as in the following, Eq. (20):

$$\bar{\theta} = 1 - \frac{2}{\pi}\cos^{-1}\left[-\frac{27}{2}\sigma^*\left(\sigma^{*2} - \frac{1}{3}\right)\right] \quad (20)$$

Thus, three specimens have been designed for tensile testing and are presented in Figure 4: one for uniaxial loading called UT0 – different to standard uniaxial specimen - and two notched specimens NT7 and NT2, with respectively a notch radius of 7 mm and 2 mm. The red dots and lines depict the extensometer location set on both experimental and numerical specimens to consider on the same basis the material elongation during the test. It captures the effective gauge length evolution regardless partial clamping or micro-sliding which could occur inside the jaws. Mechanical tests were conducted at velocity of 1 mm/min to get - for UT0 specimen only - a mean strain rate until necking of $\dot{\bar{\varepsilon}}_0 = 1.10^{-4}s^{-1}$. Tests were repeated 3 times for every specimen geometry. Dispersion between tests is bigger on cast aluminium where defects might promote an unexpected crack. Only one force-displacement curve was selected among the three, the one which handles the maximum displacement until failure. Every curves are plotted in Figure 5 (a) and (b) respectively for steel and cast aluminium.

3.1.3 In-plane shear tensile tests

In addition to uniaxial and notched specimens, an in-plane shear specimen has been designed to complete the range of investigated stress-states at fracture. Butterfly specimens were used, indicated by SH, and detailed in Figure 4. Tests have been repeated 3 times for cast aluminium and steel at the velocity of 10 mm/min.

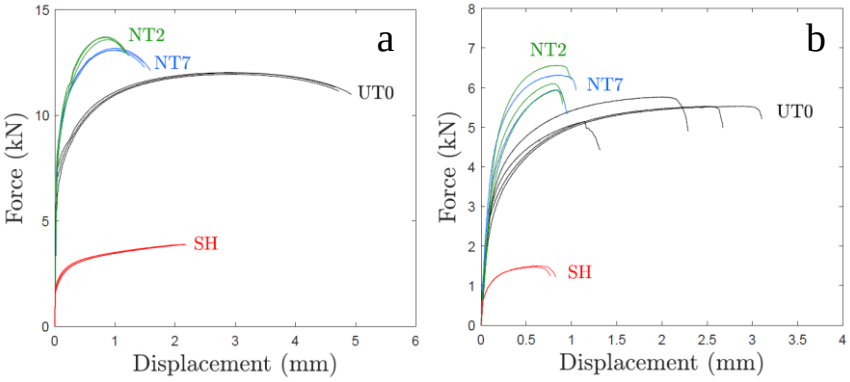


Figure 5: Experimental tensile tests conducted on four specimens geometry made of (a) steel (DP780) and (b) cast aluminium (AlSi10MnMg(T6))

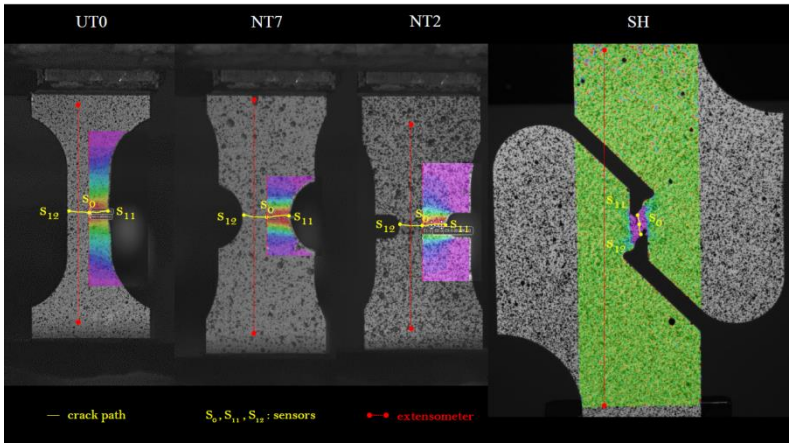


Figure 6: Quasistatic tensile test set-up including an optical measurement device for UT0, NT7, NT2 and SH sheet metal specimens (virtual extensometers and sensors are indicated by red and yellow dots and used in the post-processing step to extract local strain field).

3.1.4 Effective plastic strain at fracture

To access to the instantaneous die-displacement as well as surface strain field, a DIC optical measurement has been used for these tests. A speckle pattern was sprayed over specimens surface and virtual extensometers – pictured on Figure 6 with red dots – were positioned on specimens to measure real jaws displacements. In-plane principal strains (Hencky strains) is calculated from the displacement field obtain from the picture sequence and the effective strain $\bar{\varepsilon}$ is calculated afterward, through Eq. (21), as:

$$\bar{\varepsilon} = \sqrt{\frac{2}{3}(\varepsilon_{11}^2 + \varepsilon_{22}^2 + \varepsilon_{33}^2)} \quad (21)$$

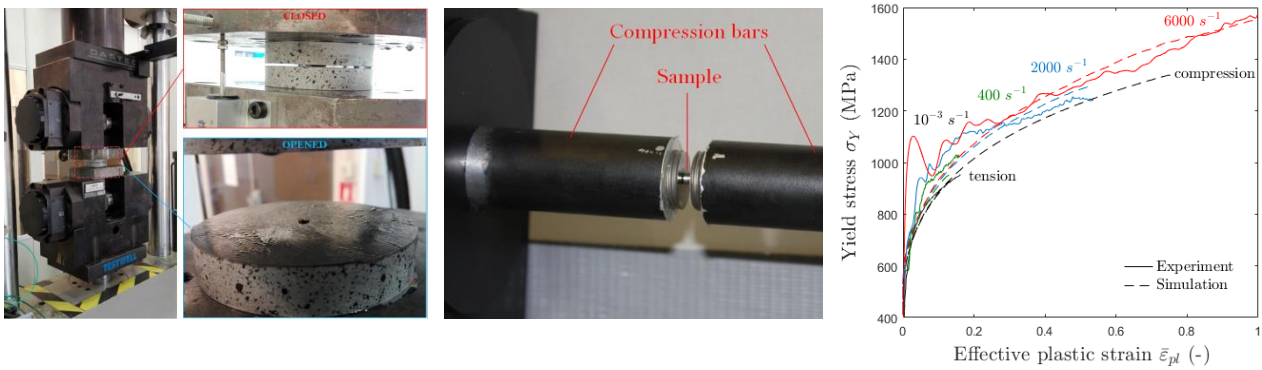
where $\varepsilon_{11}, \varepsilon_{22}$ are in-plane principal strains and ε_{33} is the strain component in the thickness direction. Plastic incompressibility is assumed and elastic strains are considered negligible regarding total strains, i.e. the relationship $\bar{\varepsilon}_{pl} = \bar{\varepsilon}$ is considered valid. As consequences, the effective strain observed in the crack onset area can be used and transformed into an effective plastic strain at fracture $\bar{\varepsilon}_f$. The identification of crack path is possible when two pictures are considered: the one just before crack has appeared and the one just after the crack has spread. Hence, sensors have been positioned on the crack path at three different spots of the specimens geometry - s_{11}, s_0, s_{12} presented in Figure 6 - and the effective plastic strain at fracture is computed. Additional informations regarding the strain field computation procedure from DIC images can be found in the Appendix.

3.1.5 Quasi-static compression tests

Steel characterization under compression loading required to extract a cylinder specimen from the 1.5 mm-thick sheet. A wire cutting machine has been used to cut a circular shape into the steel sheet and get the cylinder specimen noted C0 in Figure 4. To avoid buckling effect under compression, the cylinder diameter *d* was calibrated to be twice the height *h* (*d* = 3 mm ; *h* = 1.5 mm). Compression set-up used for this experiment is presented in Figure 7 (a).The plates were lubricated and tests were run three times at velocity 1 mm/min to get a mean strain-rate of 1.5 $10^{-2}s^{-1}$. Identical response was obtained for the three tests with a perfect overlap between curves.

3.1.6 Hopkinson-bar compression tests

To quantify strain-rate hardening and thermal softening beyond 50 s^{-1}, an Hopkinson bar test has been used.Roth (2015), Jeunechamps (2008) or Gary (2002) propose details on this test and the main principles to obtain sample stress-strain path from sensors located on both bars. Twenty-five tests have been performed at LAMIH Laboratory, based in Valenciennes (France), on the same cylinder specimen geometry C0 used for quasi-static compression tests. Impact velocity of the input Hopkinson bar was parametered to load the specimen at five different strain-rates : 400s^{-1}, 800s^{-1}, 2000s^{-1}, 3200s^{-1} and 6000s^{-1}. Each configuration has been repeated five times. Figure 7 (b) presents the Hopkinson bar set-up in which steel has been tested and Figure 7 (c) shows equivalent stress-effective strain curves in four different strain-rate configurations : 6000 s^{-1}, 2000 s^{-1}, 400s^{-1} and also10^{-3} s^{-1} to state for quasi-static reference.



(a) (b) (c)

Figure 7: (a) Quasistatic compression set-up for C0 steel specimen
(b) Hopkinson bar set-up at LAMIH for high-strain rate compression tests
(c) Experimental and numerical results from compression tests at different strain rates

3.2 Nail material characterization

As previously mentionned, the nail fastener is forged from non-alloyed carbon steel C60. Due to the manufacturing process, final properties of the nail material are far beyond the raw material ones. To quantify its properties, mechanical tests have been performed on specimens directly extracted from the nail cylindrical shaft. Three cylindrical shaft specimens of 5.13 mm, 5.13 mm and 5.6 mm (shaft diameter = 3.05mm) are subjected to compression loading until a final relative displacement of respectively 30%, 40% and 50% of the initial shaft length is reached. Compression velocity has been set to 3 mm/min for an average strain-rate of 3.10^{-2} s^{-1}. Despite lubrification of both upper and lower die, nail cylinders got deformed as a so called “barrel effect”. Such shape shows that friction is not negligible and induces an heterogeneous strain field distribution. Figure 8 shows three experimental curves and the one obtained from simulation – discussed in further section 3.3 – as well as initial and final nail shape.

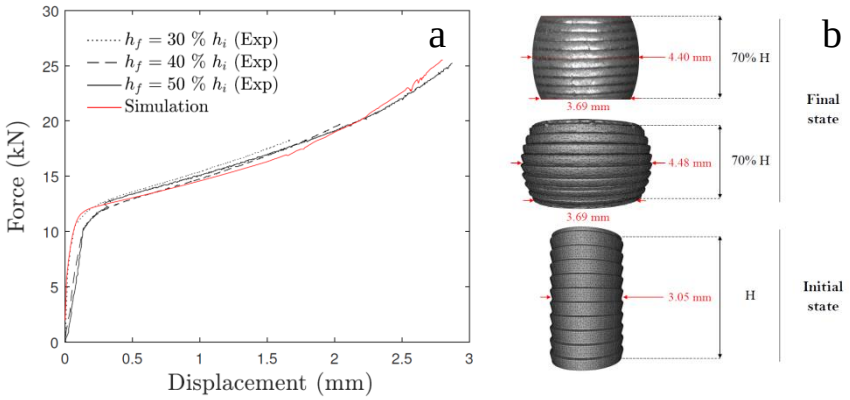


Figure 8: Comparisons between experimental and numerical compression tests performed on three nail-shaft specimens in terms of (a) force-displacement curves and (b) nail-shaft contour.

3.3 Constitutive law calibration

To properly calibrate the models according to the characterization tests performed on our materials, finite element simulation of our tests have been built with FORGE® software. The virtual extensometers displayed in Figure 4 and Figure 6 are used to consider the same gauge area in both numerical and experimental configurations. Law parameters are then optimized to obtain a mechanical response in simulation as close as possible to the one from experiment. This optimization is based on a metamodel-assisted evolutionary algorithm developped in the works of Roux (2011), coupled with FORGE®, and called MOOPI. This evaluation is done through a cost function which quantifies discrepancy between simulation and experimental curves in the least square sense.

- Sheet materials

For steel and cast aluminium, the UT0 force-displacement curve is taken as the reference for the inverse analysis procedure. Both simulations are run up to the maximum force amplitude and optimization is stopped when the best set of λ_i-parameters is found.

For strain-rate hardening parameters, a finite element model of Hopkinson compression test has been run in two different loading configurations: mean strain-rate 400 s^{-1} and 6000 s^{-1}. The optimization is applied on parameters β_1 and β_2 and the best set of parameters is validated through a third reference curve taken from a test conducted at 2000 s^{-1}. Results are plotted in Figure 7 (c) and testify the consistency of the Johnson-Cook formulation to capture strain-rate hardening of steel. Since the Hopkinson tests have been done only for steel (DP780), parameters β_1, β_2 are taken from Teng (2005) for cast aluminium considering a 2024-T351 aluminium alloy.

Thermal softening is treated in a different way for steel and cast aluminium. Since very high strain-rate implies a significant temperature increase, thermal softening can not be dissociated from the dynamic hardening. As consequences authors have considered that dynamic-thermal competition on yield stress can be well captured only with the two coefficients (β_1, β_2) calibrated from Hopkinson tests. For DP780 steel, these coefficients have been evaluated and thermal parameter is set to $\theta_1 = 0$ whereas for cast aluminium they have been taken in the literature from the works of Teng (2005) on 2024-T351 alloy.

- Nail-shaft material

As mentionned in section 3.2, a compression set-up has been used to test nail-shaft mechanical behavior. Former described procedure were also used to simulate shaft compression phase – using MOOPI software – until a satisfying set of parameters is obtained. Friction coefficient has been set to ensure that “barrel effect” is captured by simulation independantly from material parameters identification. A Coulomb-limited Tresca model was

chosen to state for friction with parameters ($\mu = 0.2$; $\bar{m} = 0.7$) where μ and $\bar{m}$ are respectively Coulomb and Tresca friction coefficients. It can be seen on Figure 8 that good agreement is obtained between experimental and numerical force-displacement curves and attests the consistency of the nail material constitutive model. Every constitutive model parameters are summed up in Table 4.

Table 4

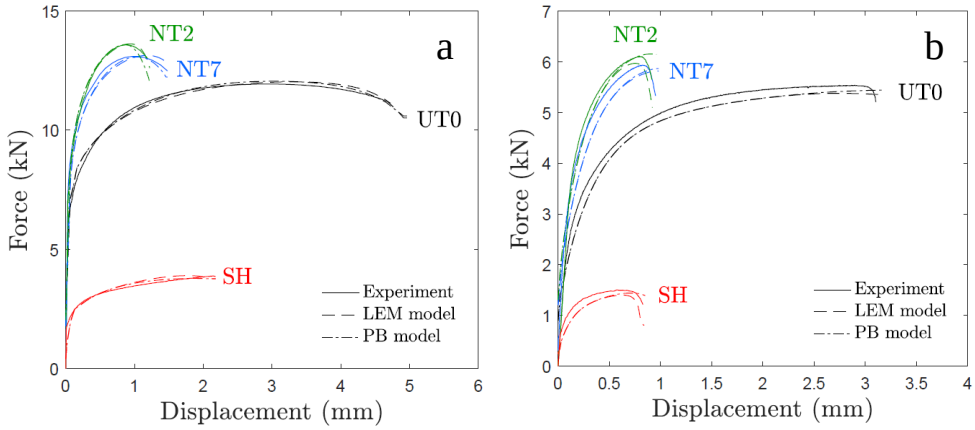


Figure 9: Comparisons of force-displacement curves obtained on (a) steel (DP780) and (b) cast aluminium (AlSi10MnMg(T6)) from experimental and numerical tensile tests computed with LEM and PB calibrated models.

3.4 Damage law calibration

Since damage growth is assumed to affect material behavior and softens its mechanical response, mechanical tensile tests were found appropriate for the calibration of the damage evolution laws. Although this coupled-damage approach is highly mesh-sensitive the calibrated law is considered valid as long as the mesh-size is identical to the one used for calibration. Consequently, in this section, the damage parameters obtained after calibration on tensile test simulation are limited to be used for applications in which mesh-size is set to 0.1 mm.

In the following subsections are presented the parameters identification procedure applied to LEM and PB coupling parameters and the construction methodology of the fracture loci.

- Lemaitre (LEM) model

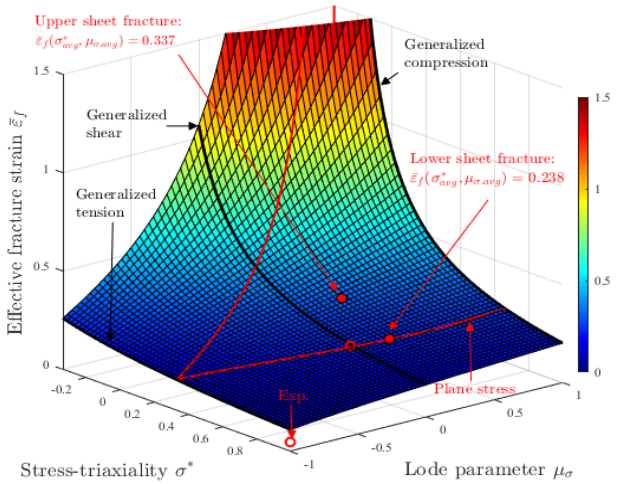
Tensile tests simulations performed on several specimens geometry have been used for the calibration of steel and cast aluminium LEM models. For cast aluminium, only NT2 tensile simulation is used as reference. The parameters to calibrate are S, b and the strain threshold values $\bar{\varepsilon}_{Di}$ corresponding to the tested stress-state ${\sigma^*}_i$. For instance, the average stress-state of NT2 specimen is ${\sigma^*}_{4\,.avg} = 0.58$ in the strain localization area. Consequently the associated strain threshold triggering damage accumulation to calibrate is $\bar{\varepsilon}_{D4}$. Once these parameters (S, b, $\bar{\varepsilon}_{D4}$) have been calibrated the other three strain threshold have to be found ($\bar{\varepsilon}_{D1}, \bar{\varepsilon}_{D2}, \bar{\varepsilon}_{D3}$) to reconstruct the locus presented in Figure 2. It is done through three independent tensile simulations respectively conducted on UT0, NT7 and SH specimens. The strain threshold value is modified gradually until the overlap between numerical and experimental force-displacement curves is satisfactory. An equivalent procedure has been applied to the calibration of LEM model on steel using UT0 and NT2 tensile tests as references. It can be noticed on the force-displacement curves presented in Figure 9 that good agreement is globally obtained from simulations computed with LEM models, except for cast aluminium whose brittle behavior makes the abrupt decreasing slope almost impossible to capture. To avoid an excessive development on this topic, the reader interested in more details on the conditions of the inverse analysis procedure is refered to the Appendix.

Table 5

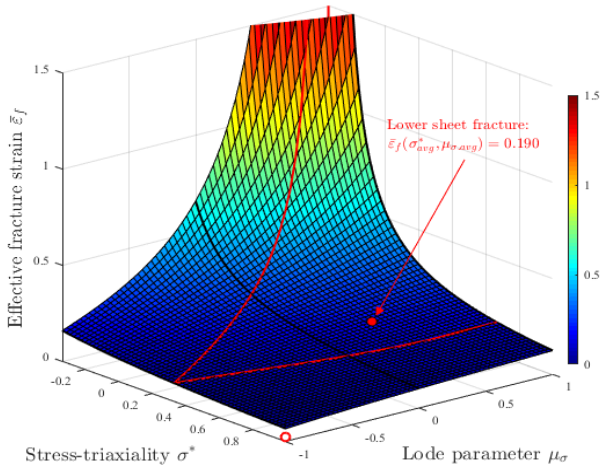
- Fracture locus calibration

Assuming a proportional loading path to fracture, the tensile test simulation computed with LEM model was used to quantify the mean-stress state $(\sigma^*_{avg}; \mu_{\sigma.avg})$ of sensors located at different spots of the crack path. A wide range of stress-states is covered by the tested specimen geometries, from $\sigma^*_{avg} = 0.07$ for SH's to $\sigma^*_{avg} = 0.57$ for NT2's. Hence it becomes possible to assign a mean stress-state to fracture – obtained from simulation - to the measurement of effective plastic strain at the specimen surface - obtained from experiment – and therefore calibrate the fracture loci on these data-points. Table 5 presents what are the data-points for every specimen and material. Since Matlab® optimization algorithm requires as many data-points as parameters to identify, it has been necessary for some criteria to add "optimization bounds" to the actual set of data-points given by experiments. It consists in additional fracture points, acting like "virtual experiments", considered in High Stress Triaxiality (HST) conditions, i.e. when the stress-state is $\sigma^* = 1$. Two cases of virtual loading path are chosen: (1) the generalized tension state, written HST-tension (HST-t), when Lode parameter is set to $\mu_\sigma = -1$, and (2) the generalized compression state, written HST-compression (HST-c) when $\mu_\sigma = +1$. From the consideration of a decreasing fracture strain with stress-triaxiality, selected values for both HST-t and HST-c data-points had to be lower than the one obtained in experiment with NT2 specimen. Thus the HST-t value has been chosen to be ½ of the HST-c fracture strain value to promote the fracture locus asymmetry regarding the Lode parameter axis. This ratio is not arbitrary; it is consistent with results from Cao (2017) on micro-mechanical representative cell in which strain to localization for X100 steel in HST-compression is about twice the HST-tension one. Similar ratio on ductility is considered valid according to the works of Barsoum and Faleskog (2011) and also Cao et al.(2015) on micro-mechanical calculation in the range of stress-triaxiality $(\sigma^* \leq 1.5)$. It appears that this gap becomes negligible under very high stress-triaxility $(\sigma^* > 1.5)$ which brings back symmetry to the fracture locus.

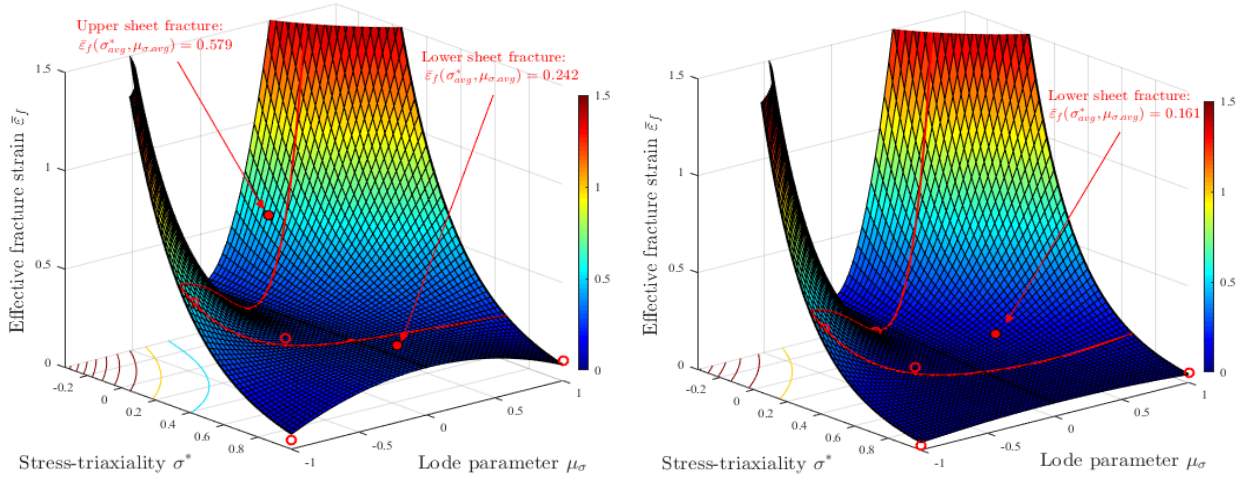
The CL, BW4P and BW6P fracture loci have been calibrated from different set of data-points taken from Table 5. Results are presented under the form of fracture surface in Figure 10 (a) and (b) for the CL criterion applied to steel and cast aluminium, in Figure 11 (a) and (b) for BW4P's, in Figure 12 (a) and (b) for BW6P's and the parameters values properly calibrated are gathered in Table 6.



(a)



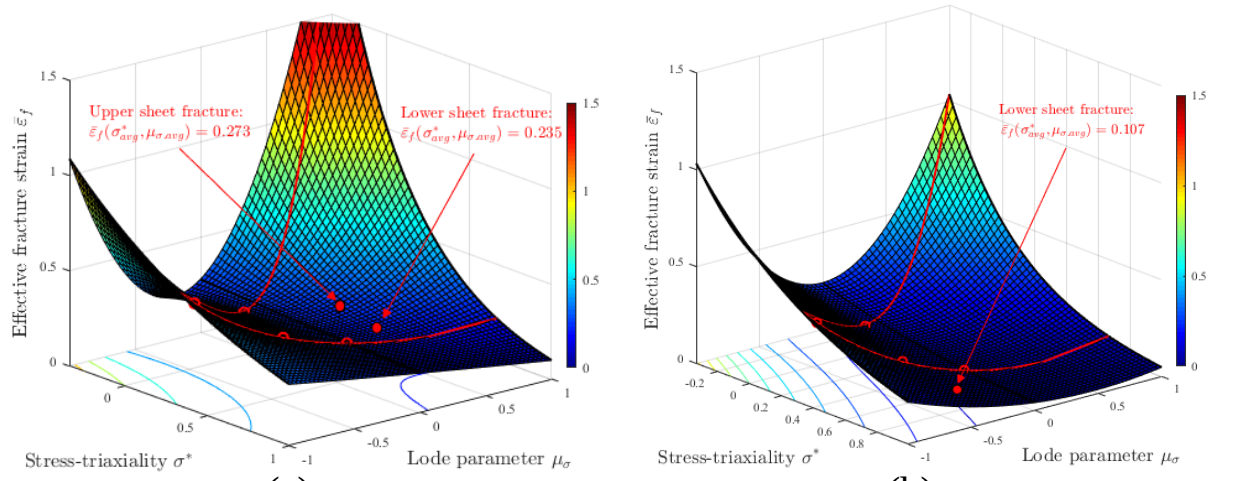
(b)



(a) (b)

Figure 10: Cockroft-Latham (CL) fracture loci for (a) steel (DP780) and (b) cast aluminium (AlSi10MnMg(T6))

Figure 11: Bai-Wierzbicki (BW4P) fracture loci for (a) steel (DP780) and (b) cast aluminium (AlSi10MnMg(T6)) (Mean stress-state leading to fracture of the sheet in the high-speed nailing simulation is pictured with a red filled



(a) (b)

Figure 12: Bai-Wierzbicki (BW6P) fracture loci for (a) steel (DP780) and (b) cast aluminium (AlSi10MnMg(T6)) (Mean stress-state leading to fracture of the sheet in the high-speed nailing simulation is pictured with a red filled

- Phenomenologically-based (PB) model

This PB-model is based on the formulation of a damage evolution Eq. (15), Eq. (16) which is driven by the fracture strain locus $\bar{\varepsilon}_f$. Three different criteria (CL, BW4P, BW6P) have been proposed and calibrated to be used in the weakening funtion presented in Eq. (9). The exact same inverse analysis procedure than for LEM-model has been used here to identify the PB-model coupling parameters. In addition to the strain threshold values $(\bar{\varepsilon}_{D1}, \bar{\varepsilon}_{D2}, \bar{\varepsilon}_{D3}, \bar{\varepsilon}_{D4})$ which are mandatory for both models, parameters to be calibrated for PB's are m and β. It is done only for BW4P and the optimized coupling values are therefore used for CL and BW6P criteria as

well. As it can be noticed in Figure 9 the model gives a good approximation of the steel force-displacement curves but the same issue as the one encountered by cast aluminium for LEM-model appears for PB's. All parameters of LEM and PB models can be find in Table 6.

Table 6

4. Experimental nailings

To depict dissimilar materials configurations which are consistent with multi-materials structures expected in the automotive industry, two joining configurations have been chosen: one in cast aluminium/steel superposition and the other one in steel/cast aluminium. Experimental nailings have been carefully conducted on a special clamping set-up to be preserved from environmental – i.e. boundary conditions - variability and avoid afterwards that validity of further comparisons with simulations could be contested.

4.1 Experimental set-up

All nailing tests have been achieved on the joining processes platform at IRT M2P in Metz (France). The joining setting device used is sold by Böllhoff company and commercially known as RIVTAC®. An experimental set-up has been designed to ensure full-clamping of the metal sheets while joint is being processed (see Figure 13). It consists in two main parts: the bottom one is a cylindrical steel made frame on which sheets are placed. A load cell is located under the sheets to measure clamping force as well as in-process joining force. The upper part has a central hole to enable the setting headpiece to access the upper-sheet and insert the nail. Two equivalent rings (28 mm-inner diameter ; 38 mm-outer diameter) are respectively located above and beneath the sheets to control both die-sheet contact areas. Clamping effect is achieved on metal sheets when bolts are tightened to connect both parts. To control quality of the joint, a displacement sensor is located in the setting device headpiece and records piston motion from the moment air flows into the main chamber to the moment the joint has been processed. These data provide important details on piston kinematics which are going to be helpul to quantify joining simulation accuracy.

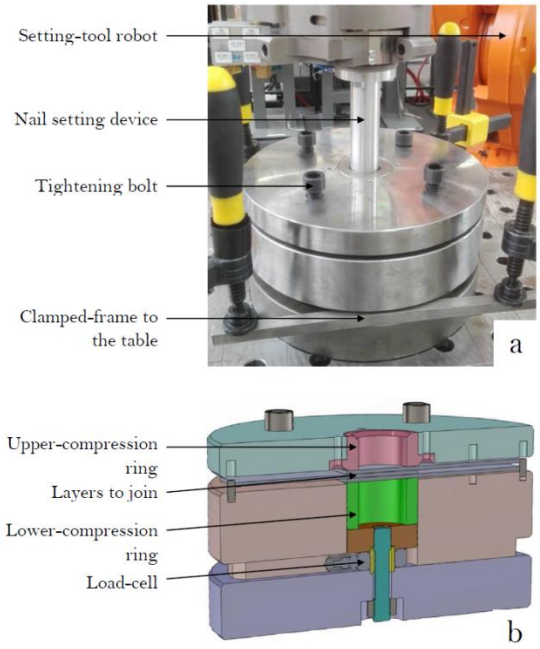


Figure 13: Experimental nailing set-up with (a) setting device in the joining position and (b) the detailed cut of the sheet clamping frame

4.2 Nailing experiment: cast aluminium/steel superposition

Seven nailing tests have been necessary to find the appropriated joining pressure to this material superposition. On the basis of experimentally-based considerations Steinig (2012) has formulated a guideline to find the appropriate process settings.Thus the optimum joining pressure for this configuration is set to 5 bars and hold-down pressure to 1 bar. Steel sheet has been positioned above cast aluminium sheet which lies on the lower ring, as pictured in Figure 13 (b). Upper frame part has been set and bolts tightened until a sheets pre-loading force of 45.4 kN was measured by the load cell.

4.3 Nailing experiment: steel/cast aluminium superposition

As in the previous configuration, seven nailings have been done before joining pressure can be optimized and set to 5.3 bars and hold-down pressure to 1 bar. Steel sheet was set-up above the cast aluminium sheet and clamped with a force of 57.3 kN.

5. Numerical simulations

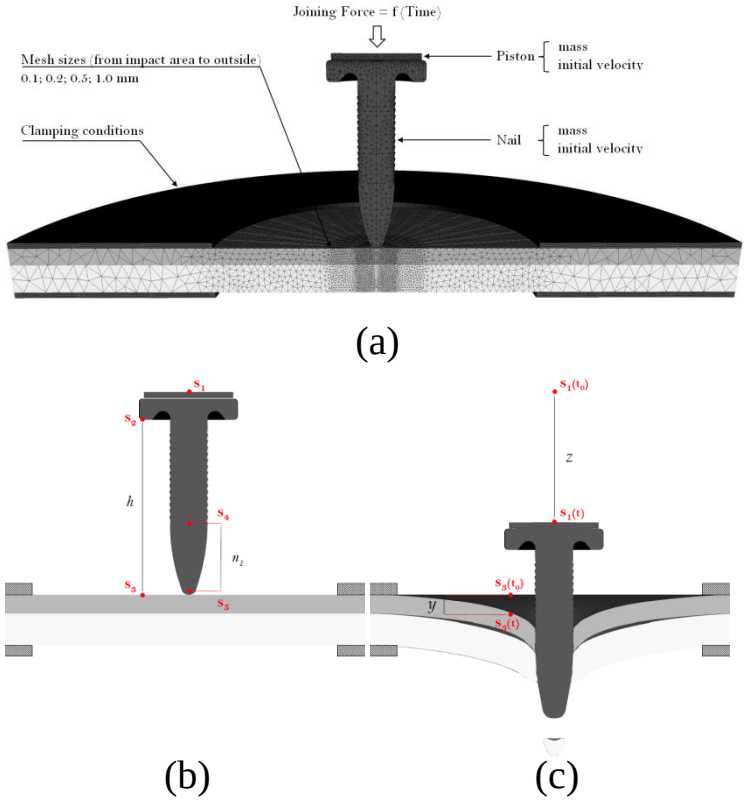


Figure 14: Model of the high-speed nailing simulation in the configuration of a 1.5 mm-thick steel (DP780) upper sheet and 2.5 mm-thick cast aluminium (AlSi10MnMg(T6)) lower sheet
(a) Summary of the mesh, loading and boundary conditions
(b) (c) Sensors s_1, s_2, s_3, s_4 and s_5 assigned to particular nodes of the mesh to compute characteristic joint dimensions $\boldsymbol{z}$, $\boldsymbol{h}$, $\boldsymbol{y}$ and $\boldsymbol{n_1}$

5.1 Finite element model

A 3D finite element model has been created with FORGE® software and applied to configurations which have already been introduced and tested in section 4.2 and 4.3. Boundary conditions as well as loading conditions

have been carefully established and modelled as presented in Figure 14 (a). Sheets are clamped between rigid rings of 14 mm inner-radius and 19 mm outer-radius. Both nail and piston initial conditions are set with a proper mass and velocity (m_{Piston} = 130 g ; m_{Nail} = 1.2 g). In addition to these conditions, an equivalent force is used to state for pressure, friction and damping effects which happened in the joining chamber during the nail insertion process (steps are detailed in Figure 1 (b)). No blank holder effect is introduced in the following simulations. To boost computation time, model is limited to a slice of 10°. Mesh size is set to 0.1 mm in the sheets impact location where damage accumulates. Since the coupled-damage approach chosen in this work is mesh-sensitive, models have been calibrated on this mesh size and therefore it is kept constant in the joining simulation. Mesh refinements has been performed on nail tip, ridges and get coarser outside of the sheets impact area. The mesh size is set to be five times bigger in the sheets bending zone than in the impact area, with at least three elements in the sheet thickness in order to ensure that bending effect is captured by simulation. Due to large deformations experienced by nail tip and metal after impact, remeshing has been necessary at every increment to catch perforation and penetration mechanisms: nail flattening, sheet stretching, blanking, fractures… Only friction between sheet and nail is considered and modelled through a Coulomb-limited Tresca formulation. From the works of Altan et al. (2005) in which a state of boundary lubrification is model through a Coulomb friction part - in which a thin organic film between metal parts is considered - and no-lubricant condition for the Tresca friction part, the parameters have been set to $\{\mu = 0\ ; \bar{m} = 0\}$ for cast aluminium-nail material interaction and $\{\mu = 0.4\ ; \bar{m} = 0.8\}$ for steel-nail material interaction. In the next section model will be changed only according to the sheet material formulations to test whereas the nail material parameters will be set to constant values - available in Table 4 -without accounting for damage.

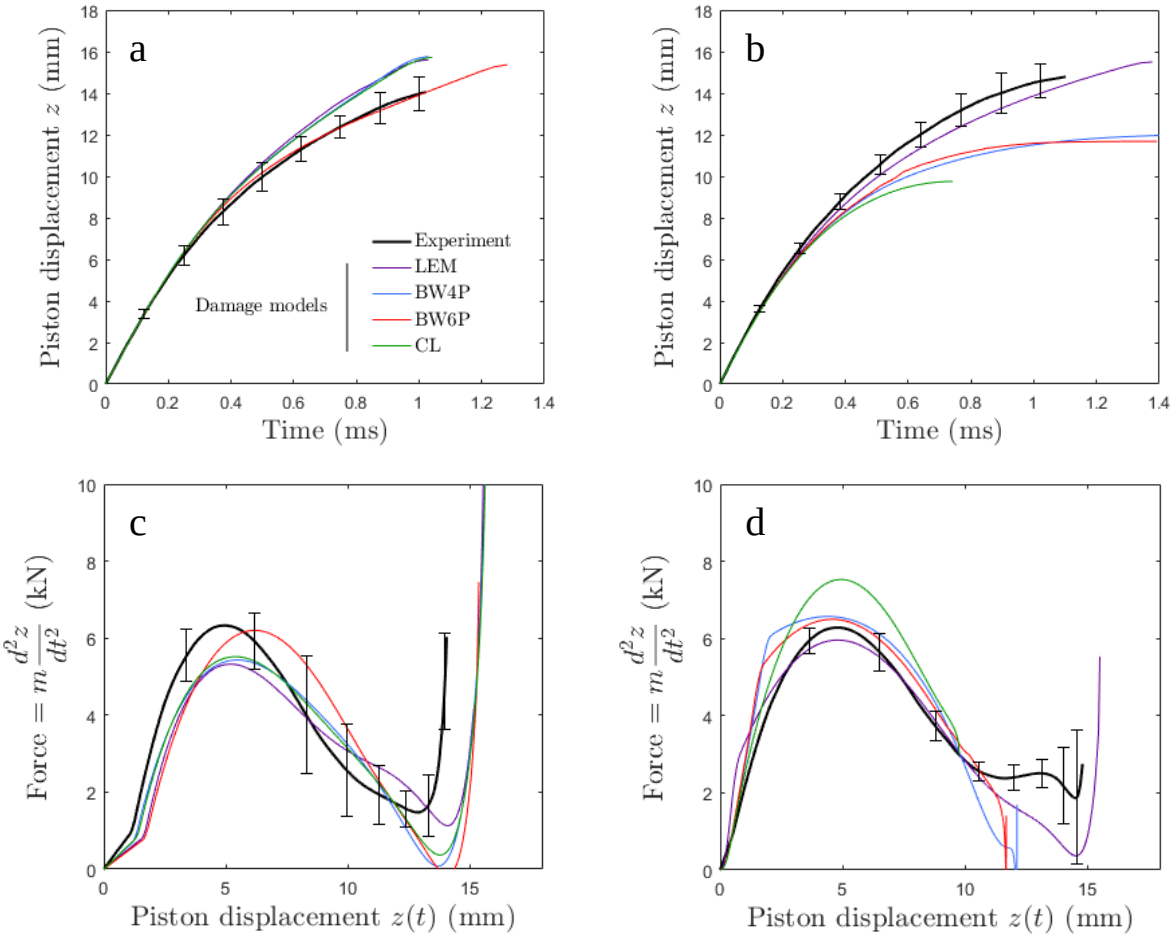


Figure 15: Piston kinematics of experimental and numerical nailing in cast aluminium/steel (a) (c) and steel/cast aluminium (b) (d) superposition

5.2 Nailing simulations: cast aluminium/steel and steel/cast aluminium superpositions

In cast aluminium/steel superposition, initial impact velocity has been set to 28.44 m/s, for both nail and piston objects, and 29.25 m/s in steel/cast aluminium. Piston motion is extracted from a node located on the symmetry axis, sensor s_1 in Figure 14, and data are then interpolated to fit experimental time series. Thus experimental and numerical piston kinematics can be computed on the same basis, within identical calculation steps: velocity and acceleration are calculated with discrete derivations over a time increment and followed with a filtering method to smooth peaks of the velocity curve. Four material fracture formulations – LEM, CL, BW4P, BW6P - have been computed and compared to experimental nailings – respectively in cast aluminium/steel and steel/cast aluminium superpositions - in Figure 15 (a) and (b) which present piston motion during the joining phase and in Figure 15 (c) and (d) in which the sheets reaction force is plotted against piston total displacement. This force is expressed as the second time derivation of piston displacement weighted by the piston mass. Experimental curve is pictured with a thick black line whereas simulations are the ones colored. It can be noticed that displacement data are plotted until the maximum piston displacement is reached and therefore the piston oscillation stage is not shown.

Among the material damage formulations tested here, one can notice on Figure 15 (a) and (b) that each formulation induces a different piston displacement path. The disparity of final piston displacement is bigger in steel/cast aluminium simulations than in cast aluminium/steel. The biggest gap with experiments occurs in both configurations with the CL-criterion whereas the best results are obtained with the BW6P's and the LEM's. Another aspect of the joining kinematics is presented in Figure 15 (c) and (d) which highlight that sheet reaction to piston motion is well captured by simulations. Maximum force amplitude discrepancy does not exceed 16% for LEM on Figure 15 (c) and 20% for CL on Figure 15 (d). Good agreement with experiment is obtained on global curve shape with an increasing force until a maximum peak is reached - in the range 5 to 6 mm in Figure 15 (c) and 4 to 5 mm in Figure 15 (d) - then followed with a decrease. Such consideration is consistent with the fact that steel sheet reliying as upper plate would have quicker effect on piston deceleration than if it was the alumimium sheet. Moreover, it can be seen on the experimental curve on Figure 15 (d) that piston stopped just after minimum has been reached whereas force keep rising in Figure 15 (c). Since the nail shaft is 14 mm long, we suggest that after an approximately 14 mm piston travel, the sheets have been fully perforated because piston has kept pushing until nail head relied on the upper sheet. No more nail displacement is possible regarding metal sheets. It implies that residual piston velocity is distributed into sheet flexion modes with a stiffer response than experienced in the perforation step.

These phenomena can be easily understood through Figure 16 which presents an insight into the nailing kinematics of both cast aluminium/steel (Figure 16 (a) (c) (e)) and steel/cast aluminium (Figure 16 (b) (d) (f)) simulations run with LEM material models. From the consideration of five sensors allocated to different nodes of the mesh (Figure 14 (b) and (c)), the distribution of the piston displacement z into three main deformation modes can be investigated through characteristic joint dimensions: nail-tip crushing distance n_1, sheet bending distance y and effective nail penetration distance h.

The time-evolution of these variables in the two configurations reveals different nail penetration mechanisms: in cast aluminium/steel, piston and nail penetration displacement rates are similar until $t = 0.1$ ms in Figure 16 (a) when the sheets are starting to bend. In the opposite configuration, a divergence between piston and nail penetration curves begins just after impact because of the sheets bending and nail-tip crushing phenomena. It means that piston displacement is mostly distributed into sheets bending and nail penetration in cast aluminium/steel configuration wheras the significant nail-tip crushing phenomenon experienced in steel/cast aluminium configuration decreases the displacement which could be actually allocated to penetration.
In other words, the nail penetration efficiency is better in cast aluminium/steel superposition than in the steel/cast aluminium one. Additional comments can be made about the sheets bending distance y and nail-tip reduction distance which have been measured – at $t = 0.6$ ms – respectively $\{y = 0.93\ mm\ ;\ n_1 = 0.10\ mm\}$ for cast aluminium/steel and $\{y = 1.35\ mm\ ;\ n_1 = 0.45\ mm\}$ for steel/cast aluminium. Hence bending distance

and nail-tip reduction are respectively 1.45 times and 4.5 times bigger in steel/cast aluminium than in cast aluminium/steel which therefore affects penetration efficiency.

The pictures taken from simulations presented in Figure 16 (e) and (f) corroborate the deformation mechanisms discussed before. They also show local aspects of sheet material fracture mechanisms such as shear plugging for both upper and lower sheets in Figure 16 (f) and only for the lower sheet in Figure 16 (e). Hence, metal sheets reaction can be illustrated using the joining steps detailed in Figure 16 (e) and (f): force increases until a maximum is reached, just before sheets have been perforated. Due to the ogival nail shape, contact area remains important with both sheets while nail keeps moving downward. At this stage, the force decreasing slope can be assigned to the petals bending resistance which slows down nail motion, as it would happen in the hole expansion test. When the hole diameter has reached nail shaft diameter, force decreasing slope is flattened and only friction plays a role in the reaction to nail descent. After joint has been processed, nail head is seated on the upper sheet as presented in both configurations of Figure 17 (a) and (b). Cross-sections from experimental nailing tests are compared with the simulations ones. It can be seen that joint final shape is globally captured by simulations, such as the remaining gap between sheets, nail crushing effect, sheets bending and the geometry at the nail-sheets interfaces. However, some local phenomena are still missing from simulations: the local bending in the nail surrounding area, the nail-tip shape and the residual distance between nail head and the upper sheet are not accurately described in Figure 17 (a) and (b) and would required additional studies to be improved.

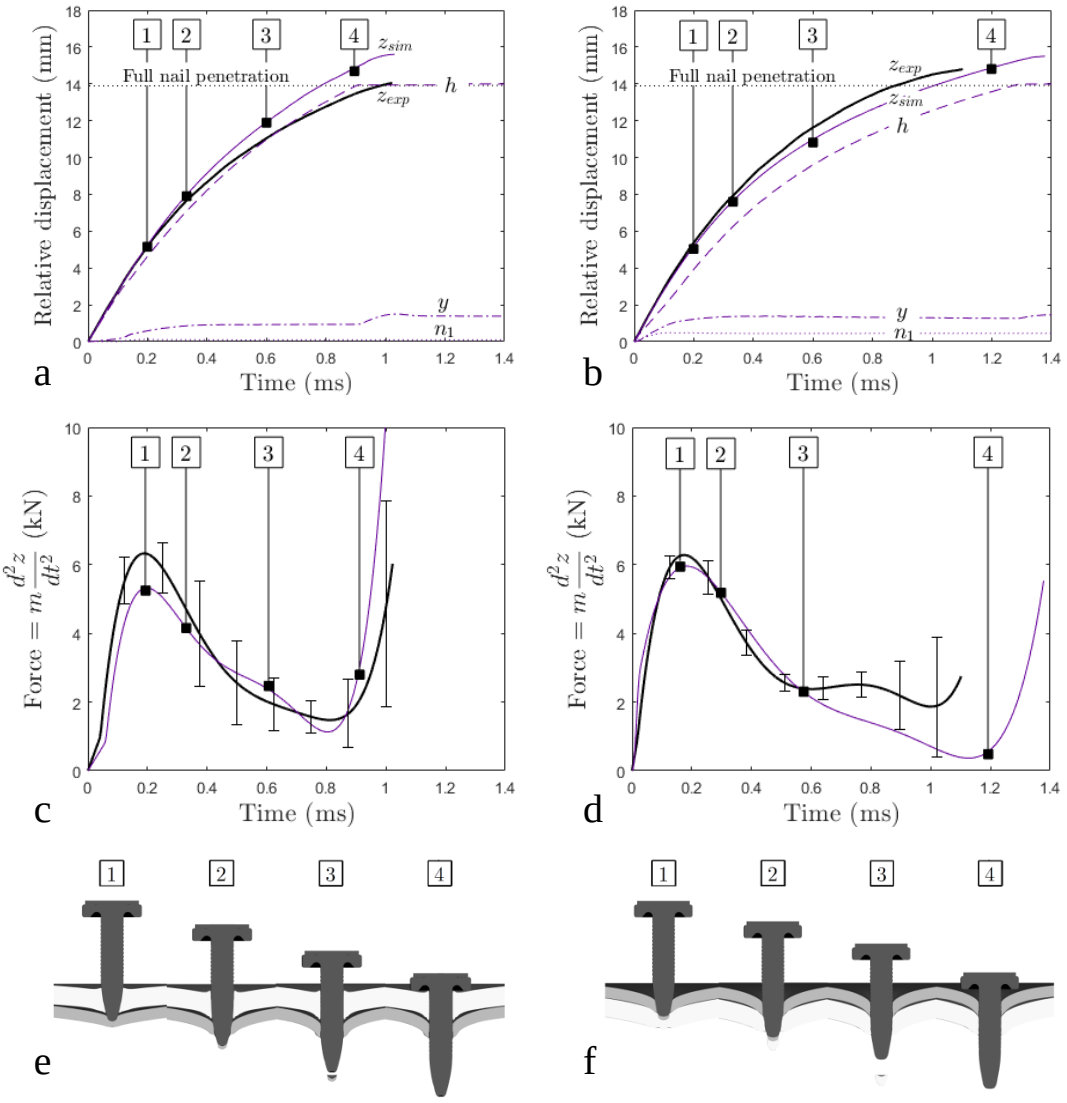


Figure 16: Detailed joining kinematics and comparisons between high-speed nailing simulations run with LEM material models and experiments on cast aluminium/steel (a) (c) (e) and steel/cast aluminium (b) (d) (f) configurations

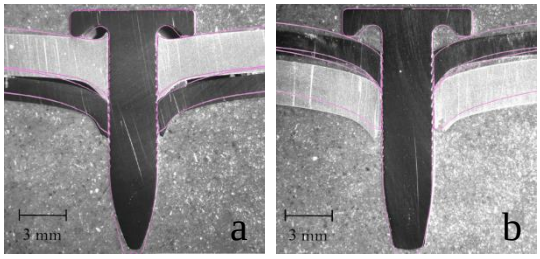


Figure 17: Comparisons between cross-sections obtained from high-speed nailing experiments and simulations with LEM material models on (a) cast aluminium/steel and (b) steel/cast aluminium configurations

5.3 Discussions from local investigations

The difference of penetration efficiency presented in Figure 16 between cast aluminium/steel and steel/cast aluminium superposition should legitimely result from the material inclination to either fracture or get an extended ductility if subjected to particular loading conditions. Hence the diagram on Figure 18 is a convenient way to investigate the reasons of these differences from a local point of view. It shows local stress-state evolution undergone by some nodes of interests: nodes located inside the sheets failure area are pictured by triangles and nodes located at the nail ridge-sheet interface are pictured by squares. It can be noticed that, except for cast aluminium/steel configuration (Figure 18 (a)) which presents stable values, stress-triaxiality can change during the perforation stage from dominant compression-state ($\sigma^* < 0$) to dominant tension-state ($\sigma^* > 0$). For conveniency, the average stress-triaxiality σ^*_{avg} has been computed on two period of the joining process: the perforation and the nail descent stages. Thus we can observe that the strain localization area in the lower sheet of cast aluminium/steel exhibits an almost constant stress-triaxiality $\sigma^*_{avg} = 0.628$ up to fracture. The upper sheet remains under an highly compression stress-state during the whole perforation steps $(\sigma^*_{avg} = -1.350)$ which confirms that damage could not grow inside the material in such conditions. On the contrary, sheet materials of the steel/cast aluminium configuration (Figure 18 (b)) undergo totally different stress-state in their strain localization area: the steel sheet bending promote through-thickness tension with an average stress-triaxiality to fracture $\sigma^*_{avg} = 0.467$. It implies that damage has to grow and propagate throughout the material in order to complete the plug separation from the sheet. It is one explanation which justify why nail penetration is slowed down when steel is position as the upper layer. The second layer, made of cast aluminium, is in a compression-state until fracture of the upper layer occurs which causes the change of stress-state into tension-dominant $\sigma^*_{avg} = 0.827$. As consequence, ductile damage process of the second layer begins only when the upper layer has failed which therefore is a second argument for a better nail penetration efficiency when cast aluminium is positioned as the upper layer.

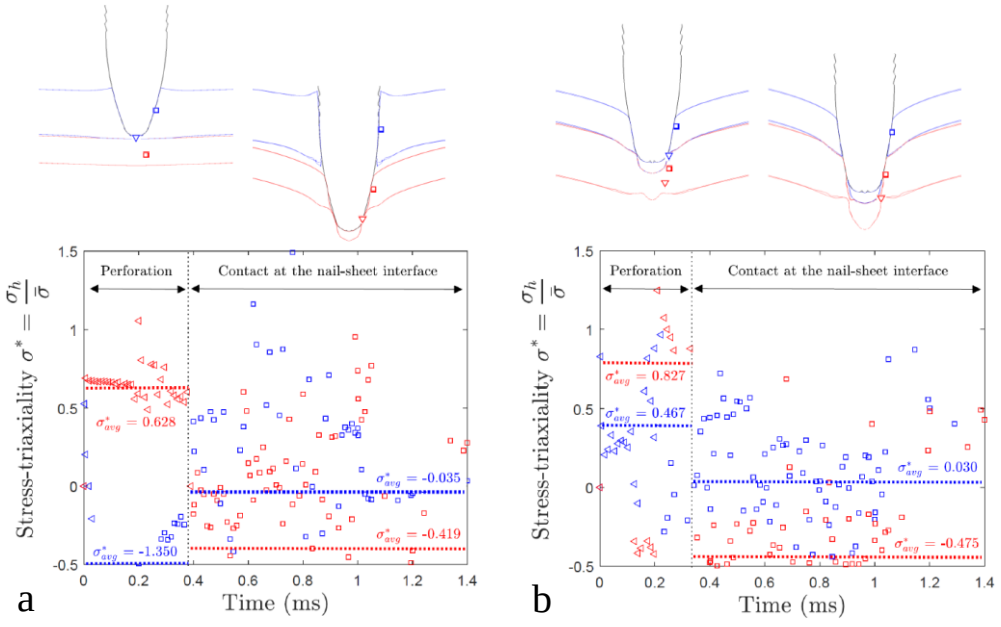
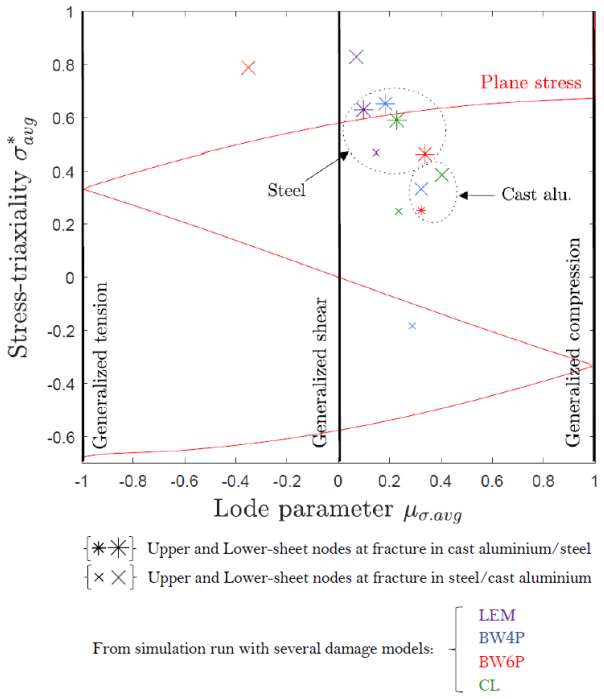


Figure 18: Stress-triaxial[illegible] during the nail insertion stage simulations - run[illegible] b) steel/cast aluminium



Remark 1: Stress-triaxial[illegible] by the effective plastic strain increment.
Remark 2: Triangles are [illegible]ail ridges-sheet contact; Blue color is used for noc[illegible] sheet)

Figure 19: Mean stress-state exhibits by nodes located in the fracture zone (pictured by triangles in Figure 18) in high-speed nailing simulations run with different damage formulations.

Remark 1: Average stress-triaxiality $(\boldsymbol{\sigma^*_{avg}})$ and Lode parameter $(\boldsymbol{\mu_{\sigma.avg}})$ values are computed from $\boldsymbol{\sigma^*}$-series and $\boldsymbol{\mu_\sigma}$-series weighted by the effective plastic strain increment.

A convenient approach to discuss the fracture conditions of metal sheets in cast aluminium/steel and steel/cast aluminum superposition modelled with different damage formulation consists in a diagram where the average Lode parameter $\mu_{\sigma.avg}$ is on the x-axis and the average stress-triaxiality σ^*_{avg} is on the y-axis. Figure 19 presents these histories for upper and lower sheet points in any damage formulations investigated before – LEM, CL, BW4P and BW6P. The reader has to refer to the particular notation specified at the bottom of Figure 19 to differentiate points from each others.

First point to notice, steel and cast aluminium sheet materials experienced very distinct stress-state histories whatever is the damage formulation. Most of the steel fracture points are located in a dominant tension region, close to the plane stress-locus, i.e. where stress-triaxiality is in the range $0.3 < \sigma^*_{avg}(\text{steel}) < 0.7$ and Lode parameter $0.1 < \mu_{\sigma.avg}(\text{steel}) < 0.35$ whereas the cast aluminium points are more scattered out of the plane-stress conditions, either in a very high-stress triaxiality region $(\sigma^*_{avg}(\text{cast alu.}) \approx 0.8)$ or close to uniaxial tension $(0.25 < \sigma^*_{avg}(\text{cast alu.}) < 0.4)$. Most of the fracture points allocated to cast aluminium positioned as upper sheet (small stars) can not be shown on the diagram due to excessive stress-triaxiality values $\sigma^*_{avg}(\text{cast alu.}) \approx -1.4$. This compression stress-state prevents the cast aluminium from damage growth and ductile failure. Hence the fracture inclination of the sheets in every tested configuration can be summed up as follows: (1) steel positioned as the upper sheet fails due to a stress-state which goes from tension to shear, far from the plane-stress condition; (2) cast aluminium positioned as the upper sheet undergoes high compression

stress-state, beyond the cut-off value ($\sigma^* < -1/3$) discussed in section 2.3 which prevents from any crack initiation and propagation. Consequently damage accumulation effect is limited and therefore the effect of damage formulation on the joining kinematics can be considered negligible as well; (3) steel positioned as the lower sheet is mostly subjected to bi-axial tension state and lies on the plane-stress locus; (4) cast aluminium positioned as the lower sheet is in a very high tension state, out of the plane-stress conditions.

Using the mean-stress state to fracture extracted from sensors in the nailing simulation, the associated fracture strain are plotted on every calibrated loci on Figure 10 (a)(b), Figure 11 (a)(b) and Figure 12 (a)(b). Despite obvious differences in the joining kinematics of cast aluminium/steel simulation (see Figure 15 (c)), no significant gap can be noticed between BW6P associated steel fracture strain $\left(\bar{\varepsilon}_f\left(\sigma^*_{avg}, \mu_{\sigma.avg}\right) = 0.235\right)$ and CL's $\left(\bar{\varepsilon}_f\left(\sigma^*_{avg}, \mu_{\sigma.avg}\right) = 0.238\right)$. Furthermore no significant difference can be noticed between joining kinematics of steel/cast aluminium simulation computed with BW6P and BW4P criteria even though their respective fracture strain values are very different: $\bar{\varepsilon}_f\left(\sigma^*_{avg}, \mu_{\sigma.avg}\right) = 0.273$ (steel) and $\bar{\varepsilon}_f\left(\sigma^*_{avg}, \mu_{\sigma.avg}\right) = 0.107$ (cast aluminium) for the BW6P criterion (see Figure 12 (a) (b)) and $\bar{\varepsilon}_f\left(\sigma^*_{avg}, \mu_{\sigma.avg}\right) = 0.579$ (steel) and $\bar{\varepsilon}_f\left(\sigma^*_{avg}, \mu_{\sigma.avg}\right) = 0.161$ (cast aluminium) for the BW4P (see Figure 11 (a) (b)). Consequently the disparity in joining kinematics can not be fully allocated to inappropriate choice of damage formulation but it should result from other aspect of the damage computation method.

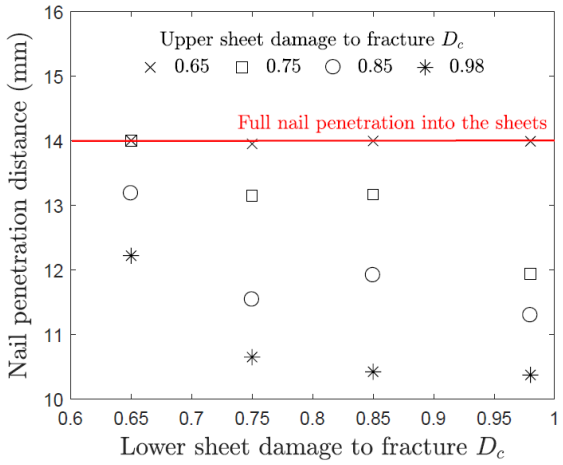


Figure 20: Influence of upper and lower sheet critical damage parameter D_c on the nail penetration distance into the sheets in steel/cast aluminium simulation run with LEM material models

5.4 Influence of critical damage parameter

In addition to the influence of fracture criteria on joining kinematics investigated through Figure 15 and Figure 19 the influence of D_c-parameter on the effective nail penetration distance is presented in Figure 20. This parameter was taken previously as $D_c = 0.98$ for cast aluminium and $D_c = 0.75$ for steel whatever are the damage formulation considered. It is usually taken as the damage value at failure in the crack onset area of the tensile test simulations. However none of the tests conducted with different specimen geometries give the same critical damage value. For instance, the calibration of LEM damage model applied to steel using UT0, NT7, NT2 and SH tensile tests gives respectively the following critical damage parameters: 0.349, 0.129, 0.345 and 0.535. But only one value has to be chosen and account for material response subjected to every possible loading path. It must be chosen carefully since it affects ductility and the nail penetration distance into the sheets. To prove this effect , sixteen simulations have been run with LEM damage model in steel/cast aluminium configuration and the nail penetration distance recorded at the end of the simulation. Both upper and lower sheet D_c parameter have been moved to values up to 0.98. Full penetration is achieved when the 14 mm-long nail shaft has traveled the whole distance, pictured by the thick red line. It can be noticed that effective nail penetration decreases when both D_c-parameters have been increased. The biggest penetration gap is obtained with the highest D_c-values: 10.35 mm instead of 14 mm. Similar comment could be done on simulations performed in cast aluminium/steel

configurations even if critical damage value doesn't affect nail penetration distance with such amplitude (further details could be found in the Appendix).

6. Conclusions

In the present work, High-Speed Nailing process has been investigated on multi-material applications composed of a 2.5 mm-thick cast aluminium sheet (AlSi10MnMg(T6)) and a 1.5 mm-thick steel sheet (DP780). Several tests have been conducted to properly calibrate material models according to their behavior under large plastic strain, high strain-rate and ductile fracture. Two kind of nailing superpositions were tested for experimental and numerical comparisons: cast aluminium/steel and steel/cast aluminium. According to results obtained from simulations, the following conclusions can be drawn:

- Whatever is the damage formulation used, in-process sheets reaction as well as piston displacement are captured by simulation. For respectively steel/cast aluminium and cast aluminium/steel superpositions, discrepancies on the maximum force amplitude do not exceed 16% and 20% (see Figure 15).
- Even if local differences can be noticed in terms of residual gap between sheets or contact distance at the interface between the upper-sheet and the nail, good agreement is obtained on global cross-sections comparisons presented in Figure 17.
- Piston displacement is not fully changed into nail insertion displacement inside the material layers. According to Figure 16 diagrams, it is distributed among three main deformation modes: sheets bending, nail-tip crushing and nail insertion depth.
- Nail penetration and perforation mechanisms are highly influenced by materials superposition: nail-tip crushing and sheets bending are bigger when upper sheet is made of steel than cast aluminium. Hence different fracture modes are promoted: shear plugging in steel/cast aluminium configuration and a mixed shear plugging-petalling in cast aluminium/steel (see Figure 16). However local investigations of stress-state evolutions inside the zone subjected to fracture reveal that, whatever is the constitutive and damage formulation used, upper-sheet failure is driven by a mixed tension-shear state, out of the plane-stress conditions, whereas the lower one is always driven by a dominant tension state, close to bi-axial tension (see Figure 18), lying in a region close to the plane-stress locus. It corroborates the characterization methodology – which covers a large range of stress-states - but it would be recommended for further improvements of the damage model calibration to also perform tests to fracture on compression specimens and various geometry of butterfly shear specimens.
- Since High-Speed Nailing is an energy-based joining process, input process parameters have to be set according to the amount of plastic work necessary to push nail until it is fully seated inside the sheets. Thus a minimum of seven experimental nailings are usually necessary to state the optimum set of input parameters of a given material configuration to join. In a way, this procedure is used to evaluate material ductility. Nailing simulations have shown that beside the consideration on the appropriate choice of damage formulation - which is not responsible for the discrepancy in the joining kinematics (see section 5.3) - the final nail penetration distance is definitely driven by parameter D_c, called critical damage parameter at fracture (see Figure 20) which controls material ductility and its value has to be set to compensate damage formulation inaccuracy.

Acknowledgements

The financial support for this work from Renault car manufacturer and the French National Association for Research-based Technology (ANRT) is gratefully acknowledged. Authors would also like to thank the Institute of Research-based Technology (IRT M2P) located in Metz for assistance and use on the experimental joining platform.

References

Abe, Y., Mori, K., Kato, T., 2012. Joining of high strength steel and aluminium alloy sheets by mechanical clinching with dies for control of metal flow. J. Mater. Process. Technol. 212, 884–889. https://doi.org/10.1016/j.jmatprotec.2011.11.015

Altan, T., Ngaile, G., Shen, G., 2005. Cold and Hot Forging: Fundamentals and Applications. ASM International.

Bai, Y., Wierzbicki, T., 2008. A new model of metal plasticity and fracture with pressure and Lode dependence. Int. J. Plast. 24, 1071–1096. https://doi.org/10.1016/j.ijplas.2007.09.004

Bao, Y., Wierzbicki, T., 2005. On the cut-off value of negative triaxiality for fracture. Eng. Fract. Mech. 72, 1049–1069. https://doi.org/10.1016/j.engfracmech.2004.07.011

Bao, Y., Wierzbicki, T., 2004. On fracture locus in the equivalent strain and stress triaxiality space. Int. J. Mech. Sci. 46, 81–98. https://doi.org/10.1016/j.ijmecsci.2004.02.006

Barsoum, I., Faleskog, J., 2011. Micromechanical analysis on the influence of the Lode parameter on void growth and coalescence. Int. J. Solids Struct. 48, 925–938. https://doi.org/10.1016/j.ijsolstr.2010.11.028

Børvik, T., Hopperstad, O.S., Berstad, T., 2003. On the influence of stress triaxiality and strain rate on the behaviour of a structural steel. Part II. Numerical study. Eur. J. Mech. - ASolids 22, 15–32. https://doi.org/10.1016/S0997-7538(02)00005-0

Bouchard, P.O., Laurent, T., Tollier, L., 2008. Numerical modeling of self-pierce riveting—From riveting process modeling down to structural analysis. J. Mater. Process. Technol. 202, 290–300. https://doi.org/10.1016/j.jmatprotec.2007.08.077

Bridgman, P.W., 1952. Studies in large plastic flow and fracture. McGraw-Hill N. Y.

Cacko, R., 2008. Review of different material separation criteria in numerical modeling of the self-piercing riveting process–SPR. Arch. Civ. Mech. Eng. 8, 21–30.

Cao, T.-S., 2017. Models for ductile damage and fracture prediction in cold bulk metal forming processes: a review. Int. J. Mater. Form. 10, 139–171. https://doi.org/https://doi.org/10.1007/s12289-015-1262-7

Cao, T.-S., Gachet, J.-M., Montmitonnet, P., Bouchard, P.-O., 2014. A Lode-dependent enhanced Lemaitre model for ductile fracture prediction at low stress triaxiality. Eng. Fract. Mech. 124-125, 80–96. https://doi.org/10.1016/j.engfracmech.2014.03.021

Cao, T.-S., Mazière, M., Danas, K., Besson, J., 2015. A model for ductile damage prediction at low stress triaxialities incorporating void shape change and void rotation. Int. J. Solids Struct. 63, 240–263. https://doi.org/10.1016/j.ijsolstr.2015.03.003

Carandente, M., Dashwood, R.J., Masters, I.G., Han, L., 2016. Improvements in numerical simulation of the SPR process using a thermo-mechanical finite element analysis. J. Mater. Process. Technol. 236, 148–161. https://doi.org/10.1016/j.jmatprotec.2016.05.001

Chastel, Y., Passemard, L., 2014. Joining Technologies for Future Automobile Multi-material Modules. Procedia Eng. 81, 2104–2110. https://doi.org/10.1016/j.proeng.2014.10.293

Cockroft, M., Latham, D.J., 1968. Ductility and workability of metals. J. Inst Mater. 96, 33–9.

Dey, S., Børvik, T., Hopperstad, O.S., Langseth, M., 2007. On the influence of constitutive relation in projectile impact of steel plates. Int. J. Impact Eng. 34, 464–486. https://doi.org/10.1016/j.ijimpeng.2005.10.003

Fayolle, S., 2009. Etude de la modélisation de la pose et de la tenue mécanique des assemblages par déformation plastique (PhD). Ecole Nationale Supérieure des Mines de Paris.

Fayolle, S., Bouchard, P.-O., Mocellin, K., 2014. Modelling the strength of self-piercing riveted joints. Woodheah Publ., Properties, Processes and Applications Self-Piercing Riveting, 79–107.

Felder, E., 2001. Effet thermique de la mise en forme - Theorie et phénomènes volumiques. Tech. Ing.

Flüggen, F., Hahn, O., 2010. Einseitiges Fügen von Blech-Profil-Konstruktionen mit lösbaren und nicht lösbaren Hilfsfügeelementen (PhD). EFB, Hannover.

Folgar Ribadas, Böddeker, Chergui, Ivanjko, Gili, Behrens, 2017. Joining TWIP-Steel simulation models. Presented at the International Conference on Structural Integrity, Structural Integrity Procedia, Funchal, Madeira, Portugal.

Gary, G., 2002. Comportement des métaux à grande vitesse de déformation: modélisation. Tech. Ing. Matér. Métalliques M3036–1.

Goldspiegel, F., Mocellin, K., Michel, P., 2017. Numerical Simulation of High-Speed Nailing Process. Presented at the 20th International ESAFORM Conference on Material Forming (ESAFORM 2017), AIP Conference Proceedings 1896, Dublin, Ireland. https://doi.org/https://doi.org/10.1063/1.5008138

Groche, P., Wohletz, S., Brenneis, M., Pabst, C., Resch, F., 2014. Joining by forming—A review on joint mechanisms, applications and future trends. J. Mater. Process. Technol. 214, 1972–1994. https://doi.org/10.1016/j.jmatprotec.2013.12.022

Gruben, G., Hopperstad, O.S., Børvik, T., 2012. Evaluation of uncoupled ductile fracture criteria for the dual-phase steel Docol 600DL. Int. J. Mech. Sci. 62, 133–146. https://doi.org/10.1016/j.ijmecsci.2012.06.009

Huang, Z., Yanagimoto, J., 2015. Dissimilar joining of aluminum alloy and stainless steel thin sheets by thermally assisted plastic deformation. J. Mater. Process. Technol. 225, 393–404. https://doi.org/10.1016/j.jmatprotec.2015.06.023
Hußmann, D., 2008. Weiterentwicklung des Bolzensetzens für innovative Fahrzeugkonzepte des automobilen Leichtbaus. Fakultät für Maschinenbau - Universität Paderborn.
International Organization for Standardization, 2009. ISO 6892-1 Metallic materials - Tensile testing - Part 1: Method of test at room temperature.
Jäckel, M., Kraus, C., Kropp, T., 2014. Effects of Increased Tool Velocity on Mechanical Joining of Steel and Aluminum Sheet Metals. Procedia CIRP 23, 24–28. https://doi.org/10.1016/j.procir.2014.10.062
Jeunechamps, P.-P., 2008. Simulation numérique, à l'aide d'algorithmes thermomécaniques implicites, de matériaux endommageables pouvant subir de grandes vitesses de déformation (PhD). Université de Liège - Faculté des Sciences Appliquées.
Johnson, Cook, 1983. A constitutive model and data for metals subjected to large strains, high strain rates and temperatures. 7th Symp. Ballist. Haye p. 541–547.
Kaboli, R., Podlesak, F., Mayr, P., 2015. Numerical simulation of spin-blind-riveting of magnesium and fibre-reinforced plastic omposite. Key Eng. Mater. 651-653, 1457–1464. https://doi.org/10.4028/www.scientific.net/KEM.651-653.1457
Lambiase, F., Di Ilio, A., 2016. Damage analysis in mechanical clinching: Experimental and numerical study. J. Mater. Process. Technol. 230, 109–120.
Lee, C.-J., Lee, J.-M., Ryu, H.-Y., Lee, K.-H., Kim, B.-M., Ko, D.-C., 2014. Design of hole-clinching process for joining of dissimilar materials – Al6061-T4 alloy with DP780 steel, hot-pressed 22MnB5 steel, and carbon fiber reinforced plastic. J. Mater. Process. Technol. 214, 2169–2178. https://doi.org/10.1016/j.jmatprotec.2014.03.032
Lemaitre, J., Chaboche, J.-L., 1994. Mechanics of solid materials, Cambridge University Press. ed.
Martinsen, K., Hu, S.J., Carlson, B.E., 2015. Joining of dissimilar materials. CIRP Ann. - Manuf. Technol. 64, 679–699. https://doi.org/10.1016/j.cirp.2015.05.006
Meschut, G., Janzen, V., Olfermann, T., 2014. Innovative and highly productive joining technologies for multi-material lightweight car body structures.
Meschut, G., Matzke, M., Hoerhold, R., Olfermann, T., 2014. Hybrid Technologies for Joining Ultra-high-strength Boron Steels with Aluminum Alloys for Lightweight Car Body Structures. Procedia CIRP 23, 19–23. https://doi.org/10.1016/j.procir.2014.10.089
Mori, K., Bay, N., Fratini, L., Micari, F., Tekkaya, A.E., 2013. Joining by plastic deformation. CIRP Ann. - Manuf. Technol. 62, 673–694. https://doi.org/10.1016/j.cirp.2013.05.004
Mucha, J., 2014. The numerical analysis of the effect of the joining process parameters on self-piercing riveting using the solid rivet. Arch. Civ. Mech. Eng. 14, 444–454. https://doi.org/10.1016/j.acme.2013.11.002
Ortiz, Camacho, 1996. Computational modelling of impact damage of brittle material. Int. J. Solids Struct. 33, 2899–2938.
Porcaro, R., Hanssen, A.G., Langseth, M., Aalberg, A., 2006. Self-piercing riveting process: An experimental and numerical investigation. J. Mater. Process. Technol. 171, 10–20. https://doi.org/10.1016/j.jmatprotec.2005.05.048
Roth, C.C., 2015. Experimental and Numerical Investigation of Ductile Fracture Initiation at Low, Intermediate and High Strain Rates (PhD). LMS, Ecole Polytechnique.
Roux, É., 2011. Assemblage mécanique: stratégies d'optimisation des procédés et d'identification des comportements mécaniques des matériaux (PhD). École Nationale Supérieure des Mines de Paris.
Schreier, H., Orteu, J.-J., Sutton, M.A., 2009. Image Correlation for Shape, Motion and Deformation Measurements. Springer US, Boston, MA.
Steinig, M., 2012. RIVTAC® : The Innovative High Speed Joining Process. Böllhoff Autom. GmbH Bielef.
Teng, X., 2005. High Velocity Impact Fracture (PhD). Massachusetts Institute of Technology.
Torsten Draht, 2006. Entwicklung des Bolzensetzens für Blech-Profil-Verbindungen im Fahrzeugbau (PhD). Paderborn university.
Wiethop, P., 2010. Stanznageln - Prozesssimulation mit Hilfe der Finiten Elemente Methode. Wiesb. Springer Fachmedien 36–40.
Zerilli, F.J., 2004. Dislocation mechanics-based constitutive equations. Metall. Mater. Trans. A 35, 2547–2555.
Zhao, S.D., Xu, F., Guo, J.H., Han, X.L., 2014. Experimental and numerical research for the failure behavior of the clinched joint using modified Rousselier model. J. Mater. Process. Technol. 214, 2134–2145. https://doi.org/10.1016/j.jmatprotec.2014.03.013

Figure and Table Captions

Table 1

Table 1: Chemical composition of 1.5 mm-thick steel sheet (DP780), 2.5 mm-thick cast aluminium ingot (AlSi10MnMg(T6)) and nail-shaft material (C60)

(% mass)	C	Mn	Mg	Si	P	S	Al	N	Ti	Mo	Cr	Ni	Cu	Zn	Fe
DP780 (1)	0,085	1,857	-	0,251	0,016	0,001	0,027	0,0046	0,002	-	-	-	-	-	-
C60 (2)	0,57-0.65	0.60 - 0.90	-	≤0.40	≤0.045	≤0.045	-	-	-	≤0.10	≤0.40	≤0.40	-	-	-
AlSi10MnMg (T6) (3)	-	0.40-0.80	0.10-0.60	9-11.5	-		-	-	≤0.20	-	-	-	≤0.05	≤0.07	≤0.25

(1) : Cast composition measurement from the steel manufacturer
(2) : C60 steel composition from standards EN-10027-1
(3) : AlSi10MnMg cast aluminium composition from standards EN AC-43500

Table 2

Table 2: Mechanical features of 1.5 mm-thick steel sheet (DP780) and 2.5 mm-thick cast aluminium ingot (AlSi10MnMg(T6))

Material	R_{p02} (MPa)		R_m (MPa)		A (%)	E (GPa)	υ	ρ (kg/m^3)
	min	max	min	max	-	-	-	-
DP780	450	550	780	900	15	194	0.33	7800
AlSi10MnMg(T6)	120	-	200	-	7	77	0.3	2700

Table 3

Table 3: Yield stress ratio $\boldsymbol{r_\alpha}$ to state for yield material anisotropy

Material	$\bar{\varepsilon}_{pl}$	$r_{0°}$	$r_{45°}$	$r_{90°}$
DP780	0.02	1	0.987	0.985
	0.04	1	0.979	0.977
	0.08	1	0.976	0.975
	0.10	1	0.976	0.975
AlSi10MnMg(T6)	Not tested			

Table 4

Table 4: Constitutive models parameters for steel (DP780), cast aluminium (AlSi10MnMg(T6)) and nail-shaft (C60) materials

	Strain hardening							Strain-rate hardening			Thermal softening [3]	
Material	λ_1	λ_2	λ_3	λ_4	λ_5	Λ	$\bar{\varepsilon}_0$	β_1	β_2	$\dot{\bar{\varepsilon}}_0$	T_m	θ_1
	(MPa)	(-)	(MPa)	(-)	(-)	(-)	(-)	(-)	(-)	(-)	(°C)	(-)
DP780	1401.7	0.199				1	$3.3e^{-3}$	$9.9e^{-10}$	$2.5e^{-3}$	$1.0e^{-3}$	1500	0
AlSi10MnMg(T6)	379.2	0.259	1.026	298.4	130.7	0.716	$3.4e^{-4}$	0	$8.3e^{-3}$ [1]	$3.3e^{-4}$ [1]	502 [1]	1 [1]
C60			614.1	763.7	150.4	0		0	0.02 [2]	$5.0e^{-4}$ [2]	1500	0

[1] : Thermal sensitivity coefficients for cast aluminium are taken from data on 2024-T351 alloy in (Teng, 2005)
[2] : No thermal sensitivity is considered for nail-shaft material with strain-rate parameters taken in the range of Weldox460E Steel's found in (Teng, 2005)
[3] : Additional parameter is set to $T_0 = 20°C$

Table 5

Table 5: Experimental and virtual effective fracture strain data-points used for the fracture locus calibration of steel (DP780) and cast aluminium (AlSi10MnMg(T6))

		Stress-state		$\bar{\varepsilon}_f$	
		σ^*_{avg}	$\mu_{\sigma.avg}$	DP780	AlSi10MnMg(T6)
EXPERIMENTAL	**SH**	0.072	-0.178	0.264	0.174
	UT0	0.353	-0.910	0.529	0.411
	NT7	0.487	-0.402	0.301	0.161
	NT2	0.569	-0.019	0.230	0.075
VIRTUAL	**HST-tension**	1	-1	0.050 [1]	0.025 [1]
	HST-compression	1	+1	0.100 [2]	0.050 [2]

Remark 1: From the consideration of the works of Barsoum and Faleskog (2011) and Cao et al. (2015), HST-t fracture strain values symbolized with [1] are assumed to be ½ the HST-c values symbolized with [2] and therefore promote assymetry of the fracture locus.
Remark 2: The set of data-points used for calibration of the fracture loci are the following: CL criterion (SH,UT0,NT2,HST-t,HST-c); BW4P criterion (SH,UT0,NT7,NT2,HST-t,HST-c); BW6P criterion (SH,UT0,NT7,NT2)

Table 6

Table 6: Lemaitre (LEM) and Phenomenologically-based (PB) damage models parameters calibrated for steel (DP780) and cast aluminium (AlSi10MnMg(T6))

Material	Damage formulation	Effective strain threshold [1]				Damage evolution and coupling [2]					Parameters of the fracture locus $\bar{\varepsilon}_f$ [3]					
		$\bar{\varepsilon}_{D1}$	$\bar{\varepsilon}_{D2}$	$\bar{\varepsilon}_{D3}$	$\bar{\varepsilon}_{D4}$	b	S [5]	m	β	D_c [4]	F_1	F_2	F_3	F_4	F_5	F_6
DP780	LEM (Eq.(12))	1.8	$2e^{-3}$	$1e^{-4}$	$2e^{-3}$	1.06	5.73		1	0.53						
	CL coupled (Eq.(17))	$1.95e^{-1}$	$5.5e^{-2}$	$5e^{-2}$	$5.5e^{-2}$			0.216	1.6		1	1	208.3			
	BW4P coupled (Eq.(18))	$1.95e^{-1}$	$5.5e^{-2}$	$5e^{-2}$	$5.5e^{-2}$			0.216	1.6	0.57	1.76	3.09	0.24	0	1.76	3.09
	BW6P coupled (Eq.(18))	$1.95e^{-1}$	$5.5e^{-2}$	$5e^{-2}$	$5.5e^{-2}$			0.216	1.6	0.61	1.01	2.33	0.26	0.23	0.80	0.91
AlSi10MnMg(T6)	LEM (Eq.(12))	$5e^{-2}$	$1e^{-1}$	$1e^{-2}$	$1.3e^{-2}$	1	0.244		1.3	0.98						
	CL coupled (Eq.(17))	$7.1e^{-2}$	$1e^{-1}$	$3e^{-2}$	$8.6e^{-2}$			0.344	1.9	0.51	1	1	128.6			
	BW4P coupled (Eq.(18))	$7.1e^{-2}$	$1e^{-1}$	$3e^{-2}$	$8.6e^{-2}$			0.344	1.9	0.71	1.80	3.77	0.14	0.72	1.8	3.77
	BW6P coupled (Eq.(18))	$7.1e^{-2}$	$1e^{-1}$	$3e^{-2}$	$8.6e^{-2}$			0.344	1.9	0.65	0.48	2.31	0.15	1.33	0.70	1.17

[1] Effective strain threshold values $\bar{\varepsilon}_{Di}$ are associated to stress-state values σ_i^* as presented in Figure 2 such as: $\sigma_1^* = 0$; $\sigma_2^* = 0.33$; $\sigma_3^* = 0.47$ and $\sigma_4^* = 0.58$.
[2] Additional micro-closure effect parameter is taken for all models as: $h = 0.2$.
[3] For conveniency, the same notation is used for fracture loci parameters $F_{i\in[1;6]}$ for BW4P's and BW6P's and only $F_{i=3}$ for CL's.
[4] Critical damage is taken at the last increment of every calibrated tensile test simulations. Only the maximum of the four values is written here. For joining simulations, this parameter is set to $D_c = 0.98$ for cast aluminium (AlSi10MnMg(T6)) and $D_c = 0.75$ for steel (DP780).
[5] Parameters are unit-free except for S which is expressed in [MPa].

Appendix A: Strain-field computation

The strain field computation is helpful to investigate strain localization and fracture process on tensile specimens but the discretization parameters have to be carefully chosen to avoid under-estimated values. As an example of the procedure followed to compute strain field in our tests, Figure X1 reveals the sensitivity of ε_{12} strain component for three sensors located in the shear localization zone of cast aluminium SH specimen at different step x filtersize. Estimated strain drops significantly if inaproppriate set of step and filtersize parameter is chosen. Therefore we have selected for our analysis step x filtersize values in the range [10;28].

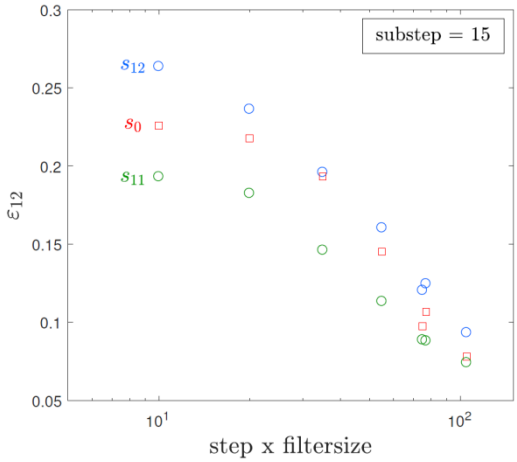


Figure X1: Evolution of the strain component ε_{12} for a given substep size obtained from VIC calculation on three sensors s_{11}, s_0, s_{12} in the shear localization zone of the cast aluminium (AlSi10MnMg(T6)) SH specimen

The effective plastic strain computed on several experimental tensile tests is used for fracture locus calibration. In the present work, the four specimens (UT0, NT7, NT2, SH) have been tested and optical measurement technic applied to compute strain field on the specimens' surface. Table X1 shows the effective plastic strain values obtained at three different location of the crack onset path for cast aluminium and steel materials.

Table X1: Effective plastic strain at fracture $\bar{\varepsilon}_f$ obtained from three DIC plane-strain measurements on UT0, NT7, NT2 and SH specimens made from cast aluminium (AlSi10MnMg(T6)) and steel (DP780) sheet materials

$\bar{\varepsilon}_f$ (Mean value ± Standard deviation)					
		UT0	NT7	NT2	SH
AlSi10MnMg(T6)	s_{11}	0.375 ± 0.251	0.109 ± 0.083	0.131 ± 0.024	0.118 ± 0.032
	s_0	0.411 ± 0.144	0.161 ± 0.097	0.075 ± 0.015	0.097 ± 0.025
	s_{12}	0.209 ± 0.128	0.255 ± 0.195	0.115 ± 0.033	0.174 ± 0.068
DP780	s_{11}	0.368 ± 0.006	0.240 ± 0.031	0.292 ± 0.016	0.224 ± 0.032
	s_0	0.529 ± 0.018	0.301 ± 0.058	0.230 ± 0.031	0.170 ± 0.042
	s_{12}	0.356 ± 0.017	0.278 ± 0.036	0.296 ± 0.032	0.264 ± 0.059

Appendix B: Material models and calibration

Once fracture locus has been calibrated, it is implemented in the PB-coupled damage formulation presented in section 2.3.2 to attest the material response on force-displacement curves in the different tensile tests. The same inverse analysis procedure has been used for the calibration of constitutive law, LEM and PB damage law parameters. It is a complex process which requires several conditions to be run and to obtain satisfactory results. As presented in Table X2, reference(s) curve(s) must be selected to quantify current discrepancy between model response and experimental reference. The initial and final domain size are respectively the number of simulations run before parameters optimization starts and the total number of simulation run for analysis. The best result is generally defined as the best cost function, associated to the best cost simulation.

Table X2: Summary of inverse analysis conditions used for calibration of the constitutive and damage models on steel (DP780), cast aluminium (AlSi10MnMg(T6)) and nail-shaft material (C60)

		DP780	AlSi10MnMg(T6)	C60
Constitutive law	Reference(s) curve(s)	UT0	UT0	cylinder shaft
	Initial domain size	40	100	60
	Final domain size	96	335	147
	Best simulation	#53	#250	#111
	Best cost function	0.055	0.041	0.073
LEM damage law	Reference(s) curve(s)	UT0, NT2	NT2	
	Initial domain size	50	50	
	Final domain size	385	111	
	Best simulation	#277	#68	
	Best cost function	0.077	0.091	
PB damage law	Reference(s) curve(s)	UT0, NT2	NT2	
	Initial domain size	50	150	
	Final domain size	138	345	
	Best simulation	#19	#304	
	Best cost function	0.078	0.124	

Appendix C: Characterization tests to check materials' model consistency

Due to heterogeneous stress-field in the C0-steel compression test, the validity of material model is checked through the force-displacement curve presented in Figure X2. Despite slight variations between simulation and experiment at the beginning and at the end of the test, good agreement is globally obtained on this test. This is consistent with results obtained from tensile tests on UT0, NT2, NT7 and SH specimens on LEM and PB coupled damage formulations.

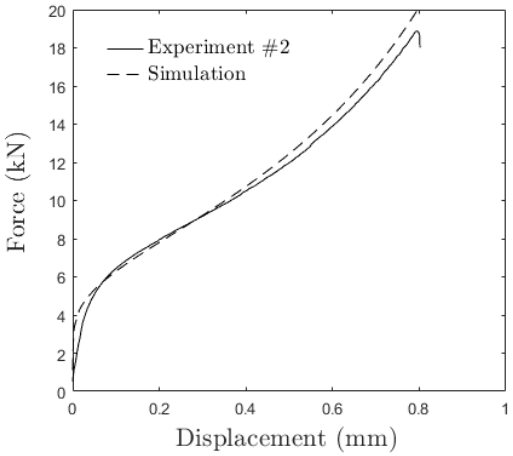


Figure X2: Comparisons between experimental and numerical force-displacement curves obtained from quasistatic compression tests conducted on C0-steel (DP780) specimen.

The whole set of experimental fracture tests have been run on a large of stress-states. Figure X3 highlights – from results of simulation run with LEM material model on steel – the average stress-state leading to fracture of crack onset area of every tested specimen. It can be noticed that mean stress-state experienced by a material point at specimen surface is different from one in the core thickness and another one in the center or in the corner of the width. These considerations should be faced to results obtained from the sheets fracture area of joining simulation for the evaluation of further characterization and fracture tests.

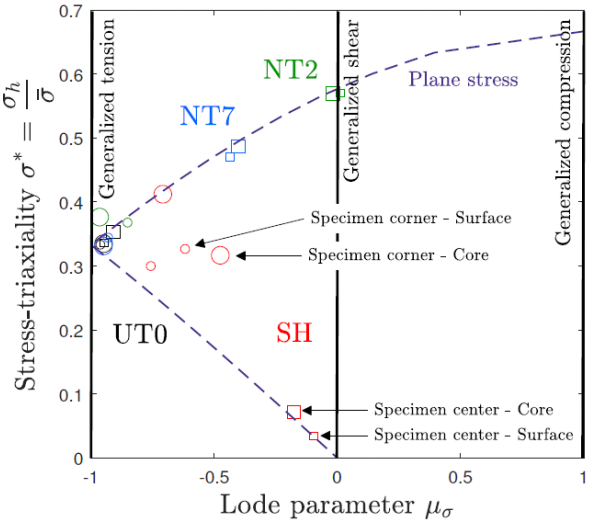


Figure X3: Mean stress-state obtained from tensile test simulations run with LEM model on steel (DP780) from sensors located in the specimens' strain localization area.
(Big symbols are assigned to a sensor located in the core thickness; small sensor for sensor at the surface; square for one at the center; circle for one at the corner/border)

Appendix D: Details regarding the high-speed nailing simulations

In the joining simulation, the stress-state analysis of strain localization area has focused on the consisderation of stress-triaxiality parameter only. It is straigthtforward for engineers and researchers to suggest what is the dominant loading state but is not sufficient to properly define a stress-state; the Lode parameter evolution should be also taken into account. Therefore it is necessary to complete the analysis which begins with Figure 18 with the following Figure X4 which states for the Lode parameter evolution during the nail insertion stage.

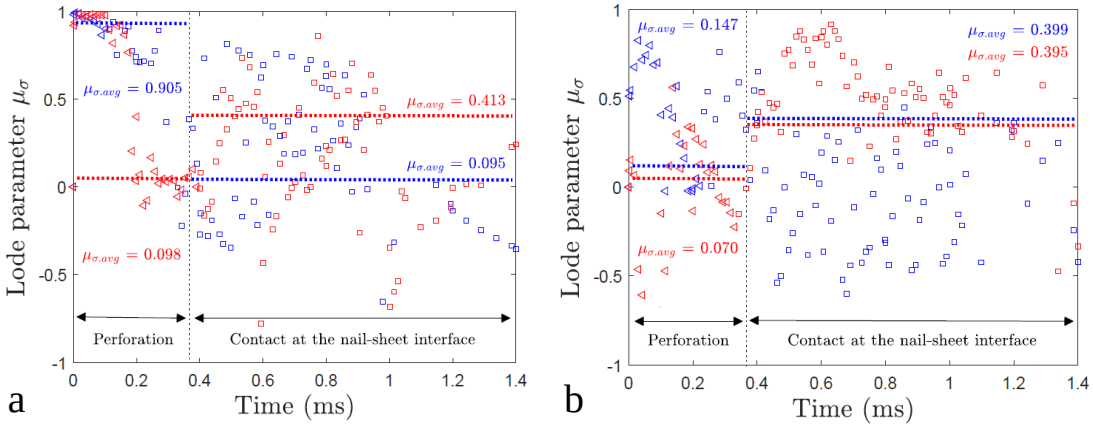


Figure X4: Lode parameter evolution exhibits by sensors located inside the two sheets during the nail insertion stage simulations - run with LEM material models - of (a) cast aluminium/steel and (b) steel/cast aluminium superposition.

Remark 1: Lode parameter average value $(\boldsymbol{\mu_{\sigma.avg}})$ is computed from $\boldsymbol{\mu_\sigma}$-series weighted by the effective plastic strain increment.
Remark 2: Triangles are nodes located in failure zone; Squares are nodes subjected to nail ridges-sheet contact; Blue color is used for nodes in the upper sheet; Red color is used for nodes in the lower sheet)

In addition to stress-state consideration, strain-rate amplitude and sheets failure sequence are also interesting data to state for the underlying mechanisms involved in the high-speed nailing process. Figure X5 uses colored-contours to indicate strain-rate localization inside the sheets at different time of the cast aluminium/steel and steel/cast aluminium joining stage.

Finally, the Figure X6 must be taken as complementary to Figure 20 and depicts a different sensitivity of the cast aluminium/steel simulation to critical damage parameter.

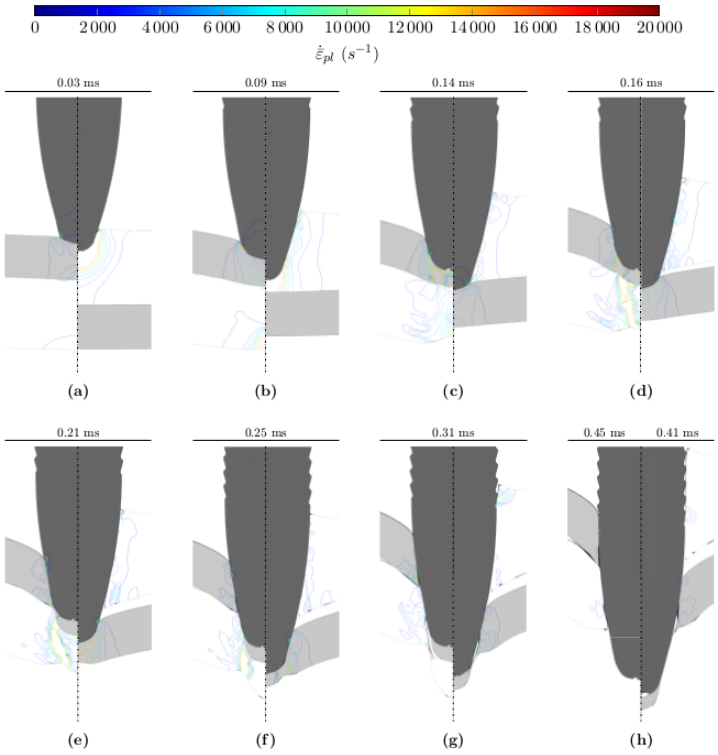


Figure X5: Evolution of the nail penetration state and the strain rate variable $\dot{\boldsymbol{\varepsilon}}_{\boldsymbol{pl}}$ in the joining stage simulation of steel/cast aluminium (Left) and cast aluminium/steel (Right) superposition computed with LEM material models.

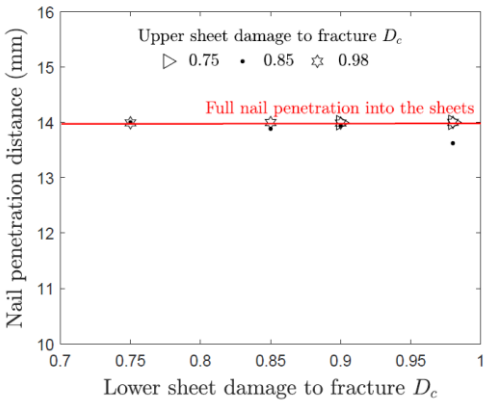


Figure X6: Influence of upper and lower sheet critical damage parameter D_c on the nail penetration distance into the sheets in cast aluminium/steel simulation run with LEM material models